



저작자표시-비영리-변경금지 2.0 대한민국

이용자는 아래의 조건을 따르는 경우에 한하여 자유롭게

- 이 저작물을 복제, 배포, 전송, 전시, 공연 및 방송할 수 있습니다.

다음과 같은 조건을 따라야 합니다:



저작자표시. 귀하는 원 저작자를 표시하여야 합니다.



비영리. 귀하는 이 저작물을 영리 목적으로 이용할 수 없습니다.



변경금지. 귀하는 이 저작물을 개작, 변형 또는 가공할 수 없습니다.

- 귀하는, 이 저작물의 재이용이나 배포의 경우, 이 저작물에 적용된 이용허락조건을 명확하게 나타내어야 합니다.
- 저작권자로부터 별도의 허가를 받으면 이러한 조건들은 적용되지 않습니다.

저작권법에 따른 이용자의 권리와 책임은 위의 내용에 의하여 영향을 받지 않습니다.

이것은 [이용허락규약\(Legal Code\)](#)을 이해하기 쉽게 요약한 것입니다.

[Disclaimer](#)



공학박사 학위논문

**Facile Synthesis and Structural
Control of Multi-component
Metallic Nanomaterials**

다성분계 금속 나노물질의

간편한 합성과 구조적 제어

2016년 8월

서울대학교 융합과학기술대학원

융합과학부 나노융합전공

최 은 진

Facile Synthesis and Structural Control of Multi-component Metallic Nanomaterials

지도 교수 박 원 철

이 논문을 공학박사 학위논문으로 제출함
2016년 4월

서울대학교 융합과학기술대학원
융합과학부 나노융합전공
최 은 진

최은진의 공학박사 학위논문을 인준함
2016년 6월

위 원 장 _____ (인)

부위원장 _____ (인)

위 원 _____ (인)

위 원 _____ (인)

위 원 _____ (인)

Abstract

Facile Synthesis and Structural Control of Multi-component Metallic Nanomaterials

Eunjin Choi

Program in Nano Science and Technology
Graduate School of Convergence Science & Technology
Seoul National University

Noble metal nanoparticles exhibit unique physical and chemical properties that are highly dependent on their size, shape, and chemical composition. During the last few decades, intensive research has been focused on the development of various synthetic methods for producing uniform nanoparticles and the precise control of their size and shape. Recently, multi-component metallic nanomaterials have attracted much

attention for their great potential application in catalysis, sensor, and biomedical application. These nanomaterials can have not only the individual characteristics of the different components, but also new and unexpected properties arising from the synergistic effect between them. In this dissertation, facile and structure-controllable synthesis of multi-component metallic nanomaterials were studied.

Firstly, Ag-Cu core-shell and alloy bimetallic nanoparticles (NPs) were prepared by a solventless mix-bake-wash method. The simple one-step heating process was assisted by salt powder as a template, obtaining small bimetallic nanomaterials. The particle structure could be controlled by tuning the annealing temperature to generate hetero-structured core-shell NPs or homogeneous alloys. Whereas the as-synthesized Ag@Cu core-shell NPs consist of a core of face-centered cubic (fcc) polycrystalline Ag NPs and a shell of fcc Cu including trace amounts of copper oxides, the AgCu nanoalloy was found to comprise a single-phase NP with the same crystal structure as that of Ag, without the copper oxide species. Cyclic voltammetric measurements confirmed the chemical identification of the surface species and their stability to oxidation.

Secondly, rattle-structured nanomaterials composed of a gold nanorod in a mesoporous silica nanocapsule (AuNR@mSiO₂) were prepared by

a novel solution-based consecutive process. Uniform-sized gold NRs were encapsulated inside a silver nanoshell, followed by SiO₂ coating through the sol-gel technique. After selectively etching away the silver inner layer, a rattle-structured nanomaterial was obtained. The AuNR@mSiO₂ rattle-shaped nanostructures were highly uniform in morphology, and the inner hollow space and the thickness of the mesoporous silica layer were easily controlled by adjusting the amount of each chemical agent. The drug-loading properties of the nanomaterial and the regrowth control of the core nanoparticles were also studied.

Keywords: Multi-component nanomaterials, noble metal, synthesis, structure control, core-shell, alloy, rattle structure.

Student Number: 2010-23946

Contents

Abstract	i
List of Figures.....	ix
List of Schemes	xxi
List of Tables.....	xxii
Chapter 1. Introduction: Various Synthetic Approaches of Multi-component Metallic Nanomaterials and Dissertation Overview.....	1
1.1 Introduction.....	1
1.2 Multi-component Metallic Nanomaterials	6
1.2.1 Various types of metal-metal and metal-silica nanostructures.....	6
1.2.2 Structure control of multi-component metallic nanomaterials.....	10
1.3 Synthesis of Multi-component Metallic Nanomaterials	14
1.3.1 Synthesis of bimetallic nanoparticles	14

1.3.2 Synthesis of rattle-structured metal-silica nanomaterials	21
1.4 Characterization of Multi-component Metallic Nanomaterials .	29
1.4.1 Transmission Electron Microscopy (TEM).....	29
1.4.2 Scanning Transmission Electron Microscopy (STEM).	30
1.4.3 Energy Dispersive X-ray Spectroscopy (EDS)	31
1.4.4 X-ray diffraction (XRD).....	35
1.4.5 X-ray photoelectron spectroscopy (XPS)	36
1.5 Dissertation Overview	41
References.....	44

**Chapter 2. Synthesis of Ag-Cu Core-Shell and Alloy
Nanoparticles via a Solventless Mix-Bake-
Wash Approach** **49**

2.1 Introduction.....	49
2.2 Experimental Section.....	52
2.2.1 Chemicals	52
2.2.2 Synthesis of Ag@Cu core-shell NPs.....	52
2.2.3 Synthesis of AgCu alloy NPs	53
2.2.4 Physicochemical characterization	53

2.2.5 Electrochemical characterization	54
2.3 Results and Discussion	55
2.3.1 Controlled synthesis of Ag-Cu core-shell and alloy bimetallic nanoparticles.....	55
2.3.2 Structural and chemical characterization.....	64
2.3.3 Investigation of the effect of salt powder on the synthesis of Ag-Cu bimetallic nanoparticles.....	71
2.3.4 Electrochemical analysis of Ag-Cu bimetallic nanoparticles.....	74
2.4 Conclusion	76
References.....	78

Chapter 3. Rattle Structured Nanomaterials of Gold Nanorod Encapsulated in Mesoporous Silica Nanocapsule for Drug Delivery and Nanoscaled Reaction 85

3.1 Introduction.....	85
3.2 Experimental Section.....	87
3.2.1 Chemicals.....	87
3.2.2 Preparation of Au nanorods.....	87

3.2.3 Synthesis of AuNR@Ag core/shell nanoparticles	88
3.2.4 Synthesis of AuNR@Ag@mSiO ₂ core/shell/shell nanoparticles.....	88
3.2.5 Synthesis of rattle-structured AuNR@mSiO ₂ core/void/shell nanoparticles	89
3.2.6 Loading of DOX.....	89
3.2.7 Regrowth of gold within rattle-structured AuNR@mSiO ₂	90
3.2.8 Characterization.....	91
3.3 Results and Discussion	92
3.3.1 Fabrication and characterization of rattle-structured AuNR@mSiO ₂ nanoparticles	92
3.3.2 Surface plasmon resonance properties	109
3.3.3 Drug loading on rattle-structured AuNR@mSiO ₂ nanoparticles.....	113
3.3.4 Chemical reactions in the void space	116
3.4 Conclusion	120
References.....	121

Chapter 4. Concluding Remarks..... 125

4.1 Conclusion	125
4.2 Future Aspects.....	128
Bibliography	130
국 문 초 록 (Abstract in Korean)	139

List of Figures

Figure 1.1 (a) Optical properties of metal NPs (Au nanorods, nanoshells, and nanocages) with different shapes, architectures, and compositions. (from Ref. [2a], Dreaden, E. C.; Alkilany, A. M.; Huang, X.; Murphy, C. J.; El-Sayed, M. A. <i>Chem. Soc. Rev.</i> 2012 , <i>41</i> , 2740.) (b) Catalytic properties of Pd NP with different crystal structure. (from Ref. [2b], Collins, G.; Schmidt, M.; O'Dwyer, C.; Holmes, J. D.; McGlacken, G. P. <i>Angew. Chem. Int. Ed.</i> 2014 , <i>53</i> , 4142.)	4
Figure 1.2 Many different possible types or morphologies of hybrid nanoparticle.	5
Figure 1.3 Schematic illustration of three possible mixing patterns in bimetallic nanoparticles: (a) core-shell structures, (b) heterostructures, and (c) alloyed nanostructures. (from Ref. [6], Wang, D.; Li, Y. <i>Adv. Mater.</i> 2011 , <i>23</i> , 1044.)	8
Figure 1.4 Schematic illustrations of various spherical rattle-structured NPs. (a) single core-shell, (b) single core-multi shells, (c)	

multi cores-single shell, (d) multi cores-multi shells, and (e)
multi-shells or shell in shell. (from Ref. [4g], Purbia, R.; Paria,
S. Nanoscale **2015**, 7, 19789.).....9

Figure 1.5 TEM images of the Ag seeds (a), the Ag@Au core-shell NPs
(b), and the Au-Ag NPs after the annealing at 100 °C for 1 h
(c) and 24 h (d). (e) UV-Vis spectra of the Ag NPs and the
Ag@Au core-shell NPs before and after annealing for 0, 1, 6,
and 24 h. (f) Photograph of the Ag-Au NP dispersions
annealed at different times. (from Ref. [11], Wang, C.; Peng,
S.; Chan, R.; Sun, S. *Small* **2009**, 5, 567.).....13

Figure 1.6 Schematic mechanism of bimetallic NPs formation during co-reduction of precursors of two different metals (M_1^{x+} and
 M_2^{y+}). (from Ref. [4k], Zaleska-Medynska, A.; Marchelek,
M.; Diak, M.; Grabowska, E. *Adv. Colloid Interface Sci.* **2016**,
229, 80.)16

Figure 1.7 (a) Powder XRD data and the selected area electron
diffraction (SAED) pattern (inset), (b) TEM image, and (c)
HRTEM image showing lattice fringes corresponding to the

111 plane of of intermetallic $\text{Au}_3\text{Ni}_{1-x}$ NPs. (from Ref. [15], Bondi, J. F.; Misra, R.; Ke, X.; Sines, I. T.; Schiffer, P.; Schaak, R. E. *Chem. Mater.* **2010**, *22*, 3988.) (d) SEM image and geometric model (inset), (e) HRTEM image and the corresponding selected-area FFT pattern (inset), (f) XRD pattern, and (g) HAADF-STEM-EDS mapping images of rhombic dodecahedral Au-Pd alloy nanocrystals. (from Ref. [16], Lee, Y. W.; Kim, M.; Kang, S. W.; Han, S. W. *Angew. Chem. Int. Ed.* **2011**, *50*, 3466.).....19

Figure 1.8 (a) Schematic illustration of single bimetallic precursor and (b) TEM image of FePt alloy NPs via thermal decomposition method. (from Ref. [17], Robinson, I.; Zacchini, S.; Tung, L. D.; Maenosono, S.; Thanh, N. T. *Chem. Mater.* **2009**, *21*, 3021.).....20

Figure 1.9 (a) Schematic illustration of the synthetic procedure for the $\text{Fe}_3\text{O}_4@\text{mSiO}_2$ rattle-structured NPs using the hard templated method. The $\text{AuNR}@\text{mSiO}_2$ rattle-structured NPs is produced by a similar procedure with $\text{Fe}_3\text{O}_4@\text{mSiO}_2$ rattle-structured NPs. (b-d) TEM images of (b) CTAB-stabilized

AuNRs, (c) PEI coated AuNR@mSiO₂ core-shell NPs, (d) PEI coated AuNR@mSiO₂ rattle-structured NPs, (e) UV/Vis absorption spectra of a) AuNRs, b) PEI coated AuNR@mSiO₂ core-shell NPs and c) PEI coated AuNR@mSiO₂ rattle-structured NPs, respectively. (from Ref. [19], Zhang, L.; Wang, T.; Yang, L.; Liu, C.; Wang, C.; Liu, H.; Wang, Y. A.; Su, Z. *Chem. Eur. J.* **2012**, *18*, 12512.) ... 23

Figure 1.10 (a) SEM and TEM (inset) images of AuAg alloy double-walled nanotubes. (from Ref. [20], Sun, Y.; Wiley, B.; Li, Z.-Y.; Xia, Y. *J. Am. Chem. Soc.* **2004**, *126*, 9399.) (b) TEM image of Au-based hollow octahedral shaped rattle nanostructures with Au NRs and (c) Schematic illustration of the procedure for preparing (b). (from Ref. [21], Cho, E. C.; Camargo, P. H. C.; Xia, Y. *Adv. Mater.* **2010**, *22*, 744.) (d) TEM and schematic images of the growth of gold nanorattles. (from Ref. [22], Khalavka, Y.; Becker, J.; Sönnichsen, C. *J. Am. Chem. Soc.* **2009**, *131*, 1871.) 27

Figure 1.11 (a) An illustration of the *in situ* confined growth of Au NRs from Au nanosphere seeds inside hollow mesoporous silica

shells. (b, c) TEM images showing hollow mesoporous silica shells containing Au (b) nanospheres and (c) NRs. (from Ref. [23], Goebel, J.; Yin, Y. *ChemCatChem* **2013**, *5*, 1287.)28

Figure 1.12 (a) TEM images of Au@Ag core-shell nanoprisms (inset: the side view of a core-shell nanoprism) (from Ref. [24], Xue, C.; Millstone, J. E.; Li, S.; Mirkin, C. A. *Angew. Chem.* **2007**, *119*, 8588.) and (b) HR-TEM image of Pd-Cu nanocrystals (from Ref. [25], Mao, J.; Liu, Y.; Chen, Z.; Wang, D.; Li, Y. *Chem. Commun.* **2014**, *50*, 4588.).32

Figure 1.13 HAADF-STEM images of (a) Au@Ag heterogeneous nanorods (from Ref. [26], Li, C.; Sun, L.; Sun, Y.; Teranishi, T. *Chem. Mater.* **2013**, *25*, 2580.) and (b) AuAg/C@SiO₂ core-shell nanoparticles (from Ref. [27], Chen, Y.; Wang, Q.; Wang, T. *Dalton Trans.* **2013**, *42*, 13940.).33

Figure 1.14 (a) HAADF-STEM image and (b-d) EDS mapping images of Au@SiO₂@Ag@SiO₂ nanoparticles, including (b) Au core: green; (c) Ag shell: yellow; and (d) double SiO₂ shells: orange. (from Ref. [29], Wang, Y.; Zhai, J.; Song, Y.; Lin, J.;

Yin, P.; Guo, L. *Adv. Mater. Interfaces* **2015**, *2*, 1500383.) 38

Figure 1.15 XRD patterns of PtCu rhombic dodecahedron and hexapod concave nanocrystals. (from Ref. [31], Liu, X.; Wang, W.; Li, H.; Li, L.; Zhou, G.; Yu, R.; Wang, D.; Li, Y. *Sci. Rep.* **2013**, *3*, 1404.) 39

Figure 1.16 XPS spectra of (a) Pd NPs, (b) Cu NPs, and (c-e) PdCu nanoparticles prepared in the different concentration of sodium dodecyl sulfate: (c) 12.5, (d) 25, and (e) 37.5 mM. (from Ref. [33], Wu, W.-P.; Periasamy, A. P.; Lin, G.-L.; Shih, Z.-Y.; Chang, H.-T. *J. Mater. Chem. A* **2015**, *3*, 9675.) 40

Figure 2.1 Digital photographs of (a) sodium sulfate powder mixed with Ag and Cu precursor solutions and ground by a mortar and pestle and (b) the powder after heat treatment at 400 °C. .. 57

Figure 2.2 SEM images of (a) sodium sulfate powder, (b) Ag-Cu bimetallic NPs on sodium sulfate powder, and (c) Ag-Cu bimetallic NPs after removal of sodium sulfate salt powder. 58

Figure 2.3 Morphological and compositional characterization of Ag@Cu core-shell NPs: (a, b) TEM images, (c) HR-TEM image, (d) FFT diffraction pattern of (c), (e) HAADF-STEM image, and (f) corresponding EDX line-scanning profiles along the line in inset.....62

Figure 2.4 Morphological and compositional characterization of AgCu alloy NPs: (a, b) TEM images, (c) HR-TEM image, (d) FFT diffraction pattern of (c), (e) HAADF-STEM image, and (f) the corresponding EDX line-scanning profiles along the line in inset.....63

Figure 2.5 XRD patterns of the synthesized (a) Ag@Cu core-shell NPs and (b) AgCu alloy NPs. The diffraction peaks ascribed to Ag, Cu, CuO, and Cu₂O are marked with the symbols ■, ◆, ▲, and ▼, respectively.65

Figure 2.6 SEM and of pure Cu NPs (a), Ag@Cu core-shell NPs with Ag to Cu molar ratios of 1:1 (b) and 1:3 (c). (d) Comparison of XRD patterns of pure Cu (I), Ag@Cu core-shell NPs with Ag to Cu molar ratios of 1:1 (II) and 1:3 (III). The diffraction

peaks ascribing to Ag, Cu, CuO, and Cu₂O are marked with
the symbols ■, ♦, ▲, and ▼, respectively.....68

Figure 2.7 TEM and HAADF-STEM images of Ag@Cu core-shell NPs
with different molar ratios of Ag to Cu; (a, c) Ag:Cu = 1:1
and (b, d) Ag:Cu = 1:3.....69

Figure 2.8 XPS patterns in the binding energy range of (a, c) Ag 3d and
(b, d) Cu 2p from (a, b) Ag@Cu core-shell NPs and (c, d)
AgCu alloy NPs, respectively.....70

Figure 2.9 (a, b) TEM images of aggregates prepared under the same
reaction conditions for AgCu alloy NPs in absence of salt
powders.....73

Figure 2.10 Cyclic voltammogram curves of Ag@Cu core-shell NPs
(black line) and AgCu alloy NPs (red line) recorded in 0.1 M
KNO₃. Scan rate: 100 mV s⁻¹.....75

Figure 3.1 TEM images corresponding to all the steps for the fabrication
of rattle-structured AuNR@mSiO₂: (a) Au NRs, (b)

AuNR@Ag core/shell (inset: STEM-EDS line scan analysis),	
(c) AuNR@Ag@mSiO ₂ core/shell/shell (inset: expanded image of the silica shell), and (d) the rattle-structured AuNR@mSiO ₂ core/void/shell.....	96

Figure 3.2 TEM images of AuNR@Ag nanoparticles with different silver shell thicknesses. The surfaces of AuNRs were coated with silver shells having thicknesses of (a) 5 nm and (b) 11 nm, obtained by adjusting the amount of AgNO₃ to 0.001 mmol and 0.01 mmol, respectively..... 97

Figure 3.3 TEM images of AuNR@Ag@mSiO₂ with different SiO₂ thicknesses. The silica shell thicknesses is (a, e) 8 nm, (b, f) 14 nm, (c, g) 17 nm and (d, h) 21 nm, respectively 98

Figure 3.4 TEM images of AuNR@Ag@mSiO₂ NPs after treatment in different etchants: (a) 6 M HNO₃, (b) 5 M NH₄OH, and (c) 5 M H₂O₂. 101

Figure 3.5 SEM image of rattle-structured AuNR@mSiO₂. 102

Figure 3.6 Photograph of the rattle-structured AuNR@SiO₂ dispersed in

aqueous solution. 103

Figure 3.7 TEM images of rattle-structured AuNR@mSiO₂ with different void space: (a) 30 nm and (b) 35 nm. 104

Figure 3.8 Low magnification of TEM images of (a) Au NRs, (b) AuNR@Ag core/shell, (c) AuNR@Ag@mSiO₂ core/shell/shell, and (d) the rattle-structured AuNR@mSiO₂ core/void/shell. 107

Figure 3.9 Particle size distribution histograms of (a) Au NRs, (b) AuNR@Ag core/shell, (c) AuNR@Ag@mSiO₂ core/shell/shell, and (d) the rattle-structured AuNR@mSiO₂ core/void/shell corresponding to Figure 3.2a-d. (<L>: mean length of nanorods, <D>: mean diameter of nanorods, and σ: size variation and relative standard deviation of nanorods) 108

Figure 3.10 UV-vis absorption spectra of (a) Au NR, (b) AuNR@Ag core/shell, (c) AuNR@Ag@mSiO₂ core/shell/shell, and (d) the rattle-structured AuNR@mSiO₂ core/void/shell

nanoparticles..... 111

Figure 3.11 (a) Macroscopic photographs and (b) UV-vis absorption spectra of the Au NRs and the AuNR@Ag core-shell solutions. Evolutions of (c) the plasmon peak wavelengths and (d) extinction intensities of the four plasmon peaks with the AgNO₃ volume, respectively. 112

Figure 3.12 UV-vis absorption spectra of (a) the DOX solution before being loaded into the rattle-structured AuNR@mSiO₂ and (b) the DOX solution after being loaded into the nanoparticles, interacting with them, and then being unloaded from the nanoparticles. (Inset: photograph of vials containing DOX solutions corresponding to the spectra in (a) and (b). The more deeply colored solutions faded to light orange, which indicates that the DOX was loaded in the rattle-structured nanomaterials.) 114

Figure 3.13 Shape evolution of gold cores grown in rattle-structured AuNR@mSiO₂. TEM and field-emission scanning electron microscopy (FE-SEM) images obtained by changing the

HAuCl₄ concentrations to (a, d) 0.03 mM, (b, e) 0.15 mM,
and (c, f) 0.6 mM. (g, h) HR-TEM images of the edge of the
regrown Au core. 118

Figure 3.14 TEM image of nanoparticles regrown from AuNRs without
silica nanocapsules. 119

List of Schemes

Scheme 2.1 Schematic of the procedure for preparing Ag-Cu NPs with different bimetallic nanostructures.	56
Scheme 3.1 Schematic illustration of the procedure for preparing the rattle-structured Au NR encapsulated within a mesoporous silica nanocapsule. Three main steps are (A) homogeneous coating of silver on the surface of Au NRs, (B) deposition of a mesoporous silica shell on the AuNR@Ag nanoparticles, and (C) selective etching of the silver inner layer using H ₂ O ₂ as an oxidant of Ag.	95

List of Tables

Table 3.1 Comparison of the loading amounts of drug on various supports.....	115
---	-----

Chapter 1. Introduction: Various Synthetic Approaches of Multi-component Metallic Nanomaterials and Dissertation Overview

1.1 Introduction

Nanomaterials are defined as materials that have particles, crystals, grains, fibers, films, or composites with at least one dimension in the range of 1-100 nm. In general, bulk materials possess constant properties regardless of their size, but nanomaterials exhibit unique physical and chemical properties as their size changes that are different from those of bulk counterparts.^[1] In particular, noble metal nanoparticles (NPs) have interesting optical and catalytic properties, depending not only on their size but also on their shape, composition, crystal structure and surface properties (Figure 1.1).^[2] These properties are attractive for great potential applications in optics, catalysis, sensor, and biomedical applications.^[3]

Early stages of nanomaterial studies have mostly focused on the development of various synthetic methods for producing uniform NPs

and the precise control over the size and shape of single NPs to tune the physical and chemical properties. However, it was gradually recognized that a single-component material usually does not fulfill all the requirements for more efficient applications. In recent years, the development of nanomaterials and engineering has led to the design of nanocomposite materials with progressively increasing levels of complexity to obtain better performances (Figure 1.2). In this regard, the spotlight of nanomaterials research is moving from single NPs towards multi-component nanomaterials having various structures, such as core-shell, core-multishell, alloy, heterostructure, rattle structure and so forth.^[4]

Multi-component nanomaterials have two advantages: (1) the integration of different functionalities of the individual components and (2) the emergence of synergistic properties arising from the interactions between the components. A typical example is the Au@SiO₂ core-shell NPs reported by Wu and Chen's group.^[5] The inner Au nanorod (NR) core dissipating absorbed NIR light energy into heat energy is suitable as a hyperthermia agent and the outer mesoporous SiO₂ shell exhibits large surface area and pore volume, thus posing itself as an effective drug delivery vehicle. By combining the two components into core-shell

structure, the single platform can be employed simultaneously in hyperthermia and chemotherapy. Additionally, the SiO_2 shell protects the AuNR core from complex biological environments and, more interestingly, the composite nanomaterial creates a new functionality: NIR laser-controlled drug release, in which the laser-converted heat dissociates the strong interactions between drug and SiO_2 , thus releasing more drug molecules. However, despite these many advantages of multi-component nanomaterials, the increased complexity makes it difficult to fabricate.

This chapter focuses on the synthetic advances in multi-component metallic nanomaterials, particularly metal-metal and metal-silica system. Firstly, various types and the importance of structure control of multi-component metallic nanomaterials are introduced. In the following section, several synthetic strategies and characterization techniques of multi-component metallic nanomaterials are reviewed. Final section is an overview of my studies on the synthetic strategies and structure control of bimetallic NPs and rattle-structured metal-silica nanomaterials.

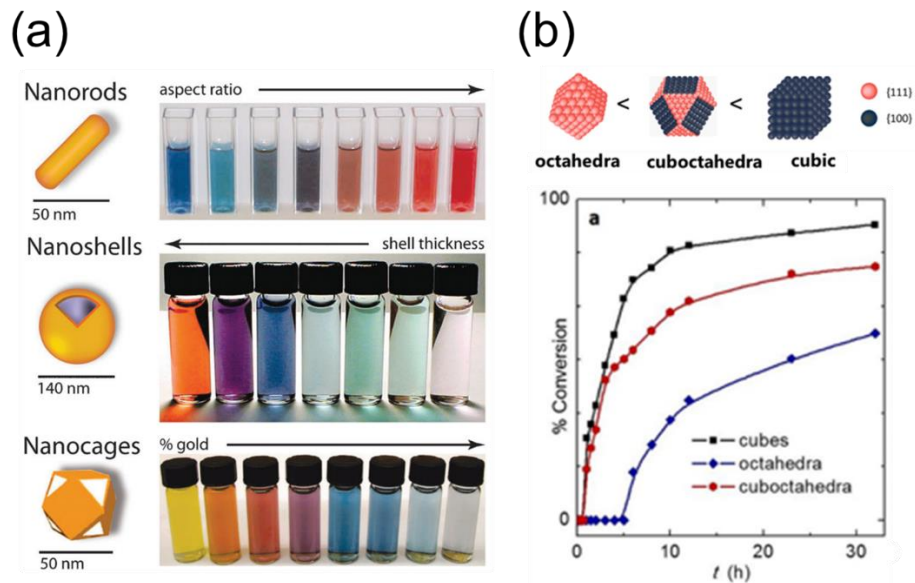


Figure 1.1 (a) Optical properties of metal NPs (Au nanorods, nanoshells, and nanocages) with different shapes, architectures, and compositions. (from Ref. [2a], Dreaden, E. C.; Alkilany, A. M.; Huang, X.; Murphy, C. J.; El-Sayed, M. A. *Chem. Soc. Rev.* **2012**, *41*, 2740.) (b) Catalytic properties of Pd NP with different crystal structure. (from Ref. [2b], Collins, G.; Schmidt, M.; O'Dwyer, C.; Holmes, J. D.; McGlacken, G. P. *Angew. Chem. Int. Ed.* **2014**, *53*, 4142.)

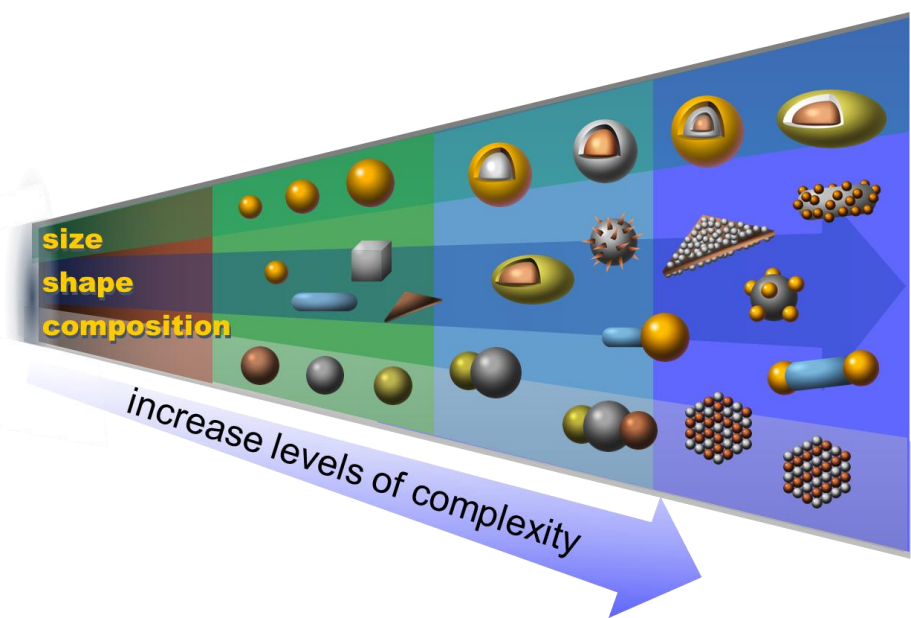


Figure 1.2 Many different possible types or morphologies of hybrid nanoparticle.

1.2 Multi-component Metallic Nanomaterials

1.2.1 Various types of metal-metal and metal-silica nanostructures

Bimetallic NPs are a class of multi-component materials which are basically composed of two different metal elements. They have not only the distinct characteristics of both component elements, but also new and unexpected properties from alloying, owing to the synergistic effects. According to Li *et al.*, bimetallic NPs can be divided in three different groups; there are core-shell structures, heterostructures, and alloyed structures (Figure 1.2).^[6] This classification depends on the different mixing patterns between the two metals. Core-shell structures consist of a shell of metal atoms surrounding a core of another metal atoms (Figure 1.2a) and heterostructures consist of two different subclusters which share a mixed interface between them (Figure 1.2b). Alloyed structures are a homogeneous mixture of two metals in either a completely ordered or a statistically random manner (Figure 1.2c).^[6-7]

As another multi-component metallic materials, metal-silica hybrid nanostructures have received considerable interest in various fields, such as sensing, imaging, therapy, and catalysis, because the addition of silica improves the thermal stability, permeability, and biocompatibility and it

does not affect the physical properties of the metal components.^[5, 8]

Metal-silica nanostructures can be available in various forms, such as core-shell, core-multi shells, and multi cores-shell, etc.^[9] Recently, rattle-structured metal-silica nanocomposites are emerging as a new class of materials that hold promise for many applications due to their unique nanostructures and excellent properties. Rattle structure can be distinguished from solid structure (with no internal porosity), core-shell structure (with a solid core wrapped by a tight layer of other element), hollow structure (with an empty inner space), Janus structure (with two hemispheres of different chemical or physical properties), as well as from reverse bumpy balls (with multiple cores grafted on the inner wall of the capsule).^[10] Rattle-structured NPs represent a hybrid structure of core-shell and hollow structure where a core particle is encapsulated inside a hollow capsule, generally forming a hierarchical core/void/shell configuration. In principle, the rattle-structured NPs consists of a single core and shell. However, their structure can be diversified by the incorporation of multi-cores and shells (Figure 1.3). Furthermore, the use of non-spherical or anisotropic metal cores instead of spherical particles leads to non-spherical rattle-structured NPs.

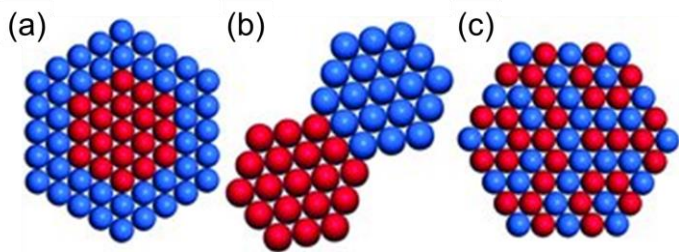


Figure 1.3 Schematic illustration of three possible mixing patterns in bimetallic nanoparticles: (a) core-shell structures, (b) heterostructures, and (c) alloyed nanostructures. (from Ref. [6], Wang, D.; Li, Y. *Adv. Mater.* **2011**, 23, 1044.)

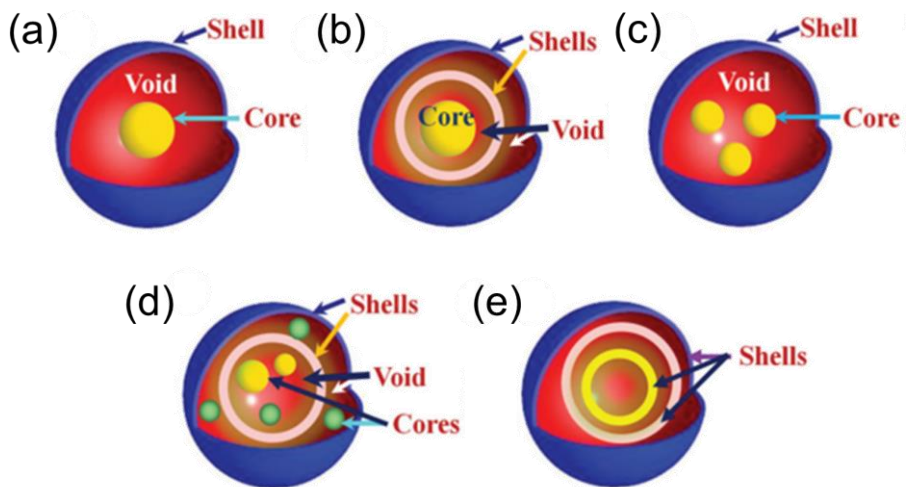


Figure 1.4 Schematic illustrations of various spherical rattle-structured NPs. (a) single core-shell, (b) single core-multi shells, (c) multi cores-single shell, (d) multi cores-multiple shells, and (e) multi-shells or shell in shell. (from Ref. [4g], Purbia, R.; Paria, S. *Nanoscale* **2015**, 7, 19789.)

1.2.2 Structure control of multi-component metallic nanomaterials

An effective structure control of multi-component metallic nanomaterials is critical to unique optical, catalytic, and synergistic properties of the materials. For example, Au-Ag bimetallic NPs show differences in optical properties depending on the structural state (Figure 1.4).^[11] Ag@Au core-shell NPs have a surface plasmon resonance (SPR) peak at 524 nm and their dispersion is dark red. Meanwhile, annealed for long time, the SPR peak of AuAg alloy NPs shifted to 460 nm indicating the mutual diffusion between Au and Ag and the dispersion changed to yellow. As another example, Mou *et al.* reported that Au-Ag alloy system shows a strong synergistic effect in high catalytic activity, compared to monometallic Au or Ag catalyst.^[12]

Furthermore, the complexity of the nanostructure can lead to multifunctionality by applying the different characteristics of each structure to one particle. Rattle structured NPs resemble core-shell structure, but they have a distinctive characteristic, which is a presence of a void between the core and the shell that provides a homogenous environment for the encapsulated core. Therefore, the rattle-structured NPs have multiple advantages such as low density, high surface area, protection of core materials, ease of interior core functionalization, large

pore volume, and excellent loading capacity in the void space, compared to core-shell or hollow structure. These properties are derived from either independent features, which are characteristic of core-shell and hollow structure, and/or synergistic effects arising from the interactions between individual structures.

Applications of rattle structured NPs in the biomedical fields can impart various functions. The void space is suitable for encapsulation of external guest molecules (e.g. fluorescent dyes, therapeutic drugs and proteins) with a specific functionality, which could be used as bio-imaging markers and drug/vaccine delivery carriers.^[13] Additionally, the core is normally composed of inorganic NPs such as magnetic oxides, noble metals, and quantum dots, which can act as magnetic resonance imaging contrast agents, photothermal agents for localized hyperthermia cancer therapy, and optical agents for biomedical imaging, respectively.^[14] The silica shell, which is the most popular materials in biomedical applications due to its good biocompatible property can be easily functionalized by well-established siloxane chemistry. In catalytic applications, a core catalyst has a high surface area and more active sites due to the presence of an unblocked surface, whereas a mesoporous shell prevents the core from agglomeration during the reaction and damages

from harsh chemical and thermal environments. Furthermore, the void space can accommodate more reactants inside the rattle-structured NPs. In this way, one particle can display multifunctionality by appropriately combining the core and the shell and controlling the interior void space.

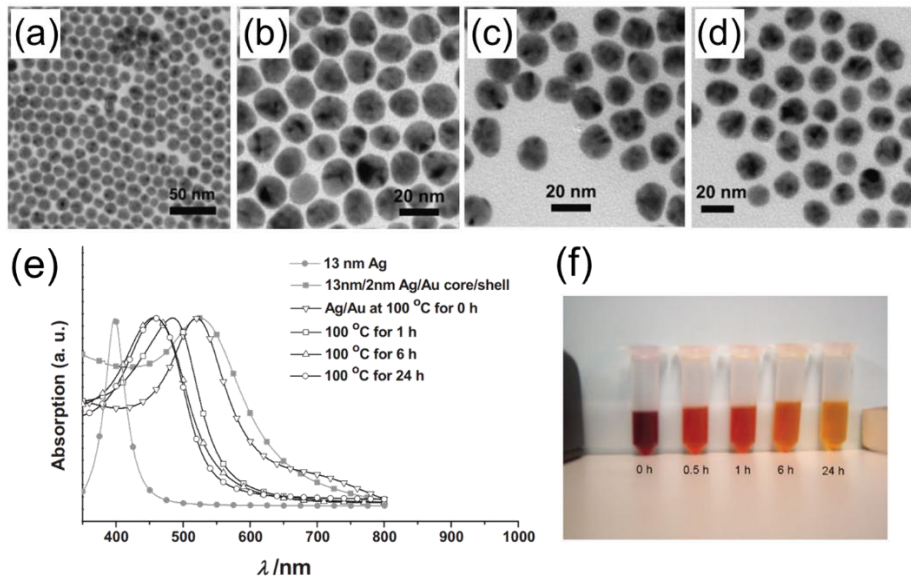


Figure 1.5 TEM images of the Ag seeds (a), the Ag@Au core-shell NPs (b), and the Au-Ag NPs after the annealing at 100 °C for 1 h (c) and 24 h (d). (e) UV-Vis spectra of the Ag NPs and the Ag@Au core-shell NPs before and after annealing for 0, 1, 6, and 24 h. (f) Photograph of the Ag-Au NP dispersions annealed at different times. (from Ref. [11], Wang, C.; Peng, S.; Chan, R.; Sun, S. *Small* **2009**, 5, 567.)

1.3 Synthesis of Multi-component Metallic Nanomaterials

1.3.1 Synthesis of bimetallic nanoparticles

The formation of noble metal-based alloy NPs is commonly more complicated than monometallic NPs. The degree of mixing and atomic ordering depends on the relative strengths of the bond between different elements, surface energies, relative atomic sizes, crystal structure of each components, strength of binding to surface ligands, and so on.^[7] To obtain noble metal-based alloy NPs with the desired structures and properties, not only the balance of these factors but also the synthetic methods and experimental conditions are crucial. During the past decades, synthesis of noble metal-based alloy NPs has been developed under various conditions including in solution, in a gas phase, or supported onto a solid substrate matrix. In this part, solution-based chemical synthesis, such as co-reduction method and thermal decomposition method, and solid substrate-supported synthesis are introduced.

Co-reduction method is the most common method for producing noble metal-based alloy NPs. In principle, this strategy is based on the simultaneous reduction of two kinds of metal salts (Figure 1.8).^[4k]

However, it is difficult to control the co-reduction process of the metal ions because their redox potential and chemical nature are different. Two metals thermodynamically prefer to separate nucleation and growth process, which results in the production of core-shell structures or heterostructures. In order to obtain alloyed nanostructures, the reaction kinetics must be controlled using proper reducing agent and surfactant or polymeric ligands. Schaak *et al.* reported the synthesis of intermetallic Au₃Fe_{1-x}, Au₃Co_{1-x}, and Au₃Ni_{1-x} NPs using n-butyllithium as the strong reducing agent that can reduce all metal precursors at the same time (Figure 1.9a).^[15] As another example, Han *et al.* presented one-pot process for the preparation of rhombic dodecahedral Au-Pd alloy nanocrystals through co-reduction of HAuCl₄ and K₂PdCl₄ by ascorbic acid in the presence of cetyltrimethylammonium chloride as surfactant (Figure 1.9b).^[16] Surfactants play a dual role to control the kinetics of nucleation and growth process as well as prevent aggregation of the NPs. The method of co-reduction has several advantages such as easy process and no need for advanced equipment.

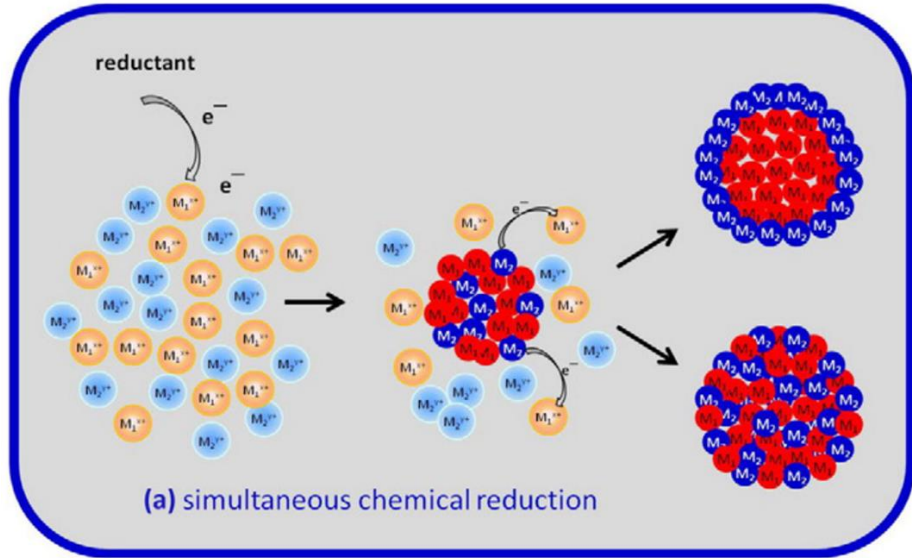


Figure 1.6 Schematic mechanism of bimetallic NPs formation during co-reduction of precursors of two different metals (M_1^{x+} and M_2^{y+}). (from Ref. [4k], Zaleska-Medynska, A.; Marchelek, M.; Diak, M.; Grabowska, E. *Adv. Colloid Interface Sci.* **2016**, 229, 80.)

Noble metal-based alloy NPs can also be synthesized with thermal decomposition of organometallic compounds that combines reduction and decomposition process. These compounds are prepared by mixing two kinds of monometallic compounds containing target metal species and are heated at elevated temperature to decompose the mixture and form monodispersed alloy NPs. This approach is typically conducted in non-aqueous solutions under inert atmosphere. However, in the same manner as co-reduction method, there is also the difference in the rates of decomposition between the two metal precursors, leading to irregular nanostructures or separate monometallic phase. A few years ago, Thanh *et al.* overcame these problems by adjusting the mixed compounds to single-source molecular precursors. FePt NPs were synthesized by decomposing of $\text{Pt}_3\text{Fe}_3(\text{CO})_{15}$ as a single-source molecular bimetallic carbonyl precursor in a solution containing toluene as the solvent and oleic acid and oleylamine as the surfactants (Figure 10).^[17] Compared to co-reduction method, this method is useful in producing alloy NPs with narrow size distribution.

Whereas the methods mentioned above are the solution-based synthesis, solid substrate-supported synthetic method is solventless synthesis. The crucial point in this method is to use salts as the separating

matrix to prevent the NPs from agglomeration and sintering. After heat treatments at high temperature, the salts can be completely removed by washing the samples in water. Lui *et al.* utilized this process for phase transformation of FePt NPs.^[18] The solid substrate-supported method is simple and easily scalable for large scale production because of the low cost and simplicity of the processing procedure.

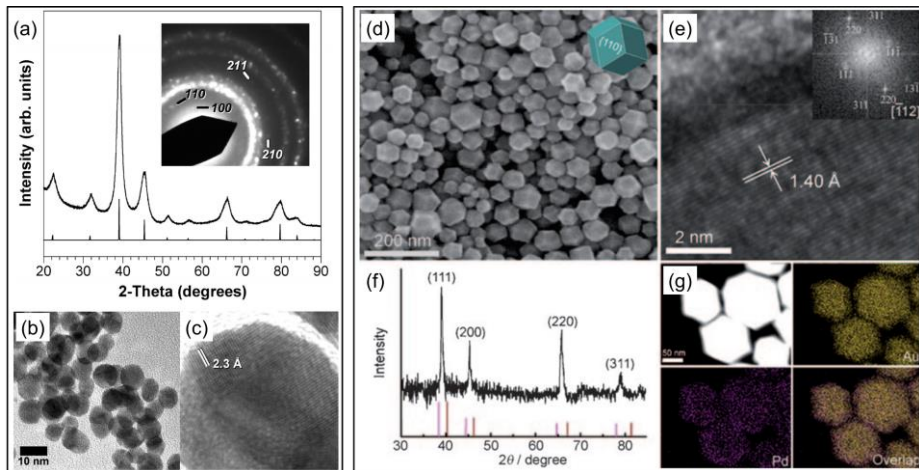


Figure 1.7 (a) Powder XRD data and the selected area electron diffraction (SAED) pattern (inset), (b) TEM image, and (c) HRTEM image showing lattice fringes corresponding to the 111 plane of intermetallic $\text{Au}_3\text{Ni}_{1-x}$ NPs. (from Ref. [15], Bondi, J. F.; Misra, R.; Ke, X.; Sines, I. T.; Schiffer, P.; Schaak, R. E. *Chem. Mater.* **2010**, *22*, 3988.) (d) SEM image and geometric model (inset), (e) HRTEM image and the corresponding selected-area FFT pattern (inset), (f) XRD pattern, and (g) HAADF-STEM-EDS mapping images of rhombic dodecahedral Au-Pd alloy nanocrystals. (from Ref. [16], Lee, Y. W.; Kim, M.; Kang, S. W.; Han, S. W. *Angew. Chem. Int. Ed.* **2011**, *50*, 3466.)

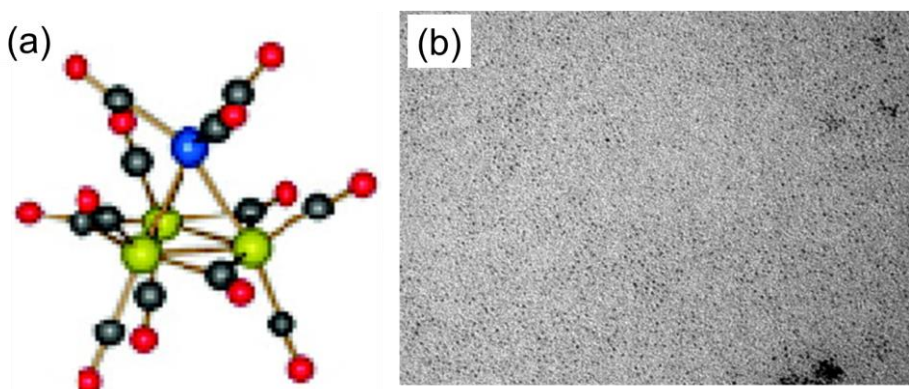


Figure 1.8 (a) Schematic illustration of single bimetallic precursor and
(b) TEM image of FePt alloy NPs via thermal decomposition method.
(from Ref. [17], Robinson, I.; Zacchini, S.; Tung, L. D.; Maenosono, S.;
Thanh, N. T. *Chem. Mater.* **2009**, *21*, 3021.)

1.3.2 Synthesis of rattle-structured metal-silica nanomaterials

Anisotropic noble metal NPs show unique optical properties different from spherical shaped particles. Because of their better performance in several applications including photothermal therapy, cancer imaging, sensor, and catalysis, anisotropic NPs have attracted researchers' attention to a large extent than spherical NPs of the same material.^[3a, 3d] In this respect, anisotropic rattle-structured NPs are no exception because of similar reasons.

With increased interest in the rattle-structured nanomaterials, a number of synthetic approaches have been developed for the preparation of these structures, such as hard template method, soft template method, galvanic replacement method, the Kirkendall reaction, template free approaches, ultrasonic spray pyrolysis, and ship-in-bottle method.^[4g] However, many of these synthetic methods have been developed for fabricating spherical nanoparticles, rather than anisotropic or non-spherical particles. Due to the complexity of the process, it's difficult to change the morphology of core or shell, thus limiting the achievable structures. Accordingly, the synthesis of non-spherical or anisotropic rattle-structured NPs remains a significant challenge.

The important steps in designing anisotropic noble metal-based rattle

structure are the maintenance of the core shape and the creation of void between the core and shell, which are key steps for fabricating the rattle-structured NPs. To the best of my knowledge, the synthetic approaches for anisotropic noble metal-based rattle-structured NPs are classified into three categories: (1) hard template method; (2) the galvanic replacement method; and (3) ship-in-bottle method.

The hard template method is the most commonly used route for synthesizing non-spherical rattle-structured NPs because of its relative simplicity of the process, ease to maintain the core shape, and control over the void space. In a typical procedure, the pre-synthesized anisotropic noble metal NPs are coated with one or several layers of hard template material, forming core-shell or core-multishell nanostructures. Subsequently, the interior shell or the middle layer is removed through dissolution with solvents, etching by acid or alkali solutions, or calcination depending on the materials properties. The crucial point in this method is to maintain the external shell layer without collapsing.

Using the hard template method, Su *et al.* reported the synthesis of rod-shaped Au@mSiO₂ rattle structures using interior silica etching after uniformly coating the core (Figure 1.4).^[19] For selective removal of interior mSiO₂ layer, polyethyleneimine (PEI) was used as a protective

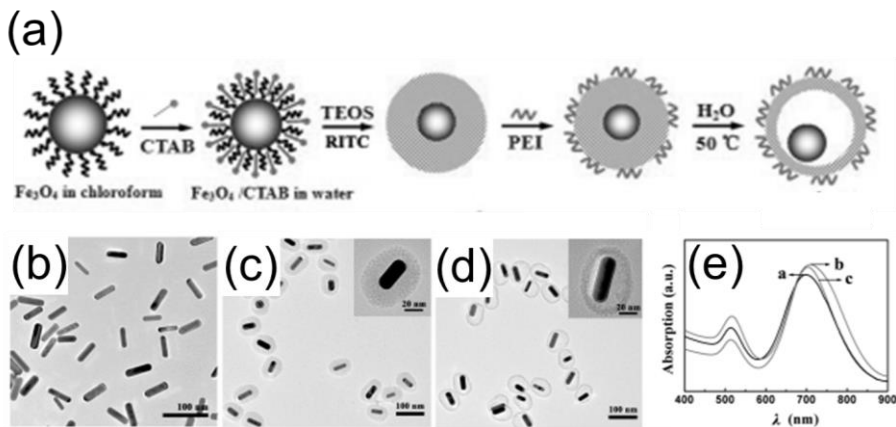
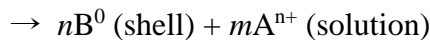
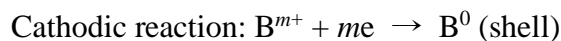


Figure 1.9 (a) Schematic illustration of the synthetic procedure for the $\text{Fe}_3\text{O}_4@\text{mSiO}_2$ rattle-structured NPs using the hard templated method. The AuNR@ mSiO_2 rattle-structured NPs is produced by a similar procedure with $\text{Fe}_3\text{O}_4@\text{mSiO}_2$ rattle-structured NPs. (b-d) TEM images of (b) CTAB-stabilized AuNRs, (c) PEI coated AuNR@ mSiO_2 core-shell NPs, (d) PEI coated AuNR@ mSiO_2 rattle-structured NPs, (e) UV/Vis absorption spectra of a) AuNRs, b) PEI coated AuNR@ mSiO_2 core-shell NPs and c) PEI coated AuNR@ mSiO_2 rattle-structured NPs, respectively. (from Ref. [19], Zhang, L.; Wang, T.; Yang, L.; Liu, C.; Wang, C.; Liu, H.; Wang, Y. A.; Su, Z. *Chem. Eur. J.* **2012**, *18*, 12512.)

layer because PEI can be deposited on the surface of the AuNR@mSiO₂ core-shell NPs through electrostatic interaction and thus prevent the dissolution of the Si-O-Si bonds at the outer layer of silica shell.

Another efficient method to prepare anisotropic noble metal-based rattle-structured NPs is galvanic replacement method. This method is based on the electrochemical potential difference between two metals, where one metal serves as the cathode, the other as the anode. Typically, atoms of a metal with low standard reduction potential (A) are deposited on the surface of core NPs, and then another metal ions with higher standard reduction potential (B) are introduced into the solution. The reaction occurs spontaneously and the middle layer (A) plays a dual role as both sacrificial template and reducing agent. The reaction can be expressed as follows:



This process is a versatile route to obtain anisotropic rattle structures with controllable shell thickness and hollow interiors, similar to a hard template method.

Xia *et al.* showed the preparation of a tubular shaped AuAg alloy rattle structure *via* a galvanic replacement reaction (Figure 1.5a).^[20] They also synthesized AuAg alloy hollow nanostructures containing Au NRs through the same reaction (Figure 1.5b and c).^[21] Another example of anisotropic rattle-structured NPs was shown by Sönnichsen *et al.* In this case, rod-shaped Au@Au rattle-structured NPs were obtained (Figure 1.5d).^[22] In all of the reports, the shell layer was formed on the surface of the Ag template because the standard reduction potential of $\text{AuCl}_4^-/\text{Au}$ pair (0.99 V vs. the standard hydrogen electrode, SHE) is higher than that of Ag^+/Ag pair (0.8 V vs. SHE).

Whereas two of the above methods are core-to-shell approaches, the last ‘ship-in-bottle’ method is shell-to-core approach. In this method, the hollow shells are synthesized first and then the cores are formed inside the hollow shells through chemical reactions or self-assembly to generate the final rattle structures. Using this method, Wang *et al.* prepared hollow mesoporous silica shells containing Au NRs by encapsulation of gold seeds inside the silica hollow shells, followed by the growth of Au NRs within the confines of the shells (Figure 1.6).^[23] Despite its conceptual simplicity and formation of complex core structures, this approach is limited by unwanted formation of core materials outside the shells which

results in low efficiency.

Most current synthetic routes to develop anisotropic noble metal-based rattle structures often involve harsh synthetic conditions, which require strong acidic or alkaline etchant or high temperature, or multistep procedures. Moreover, the control of composition and shape of the core particles is difficult and thus limited. Therefore, a facile, controllable, and effective approach to produce various non-spherical noble metal-based rattle structures is still a great challenge.

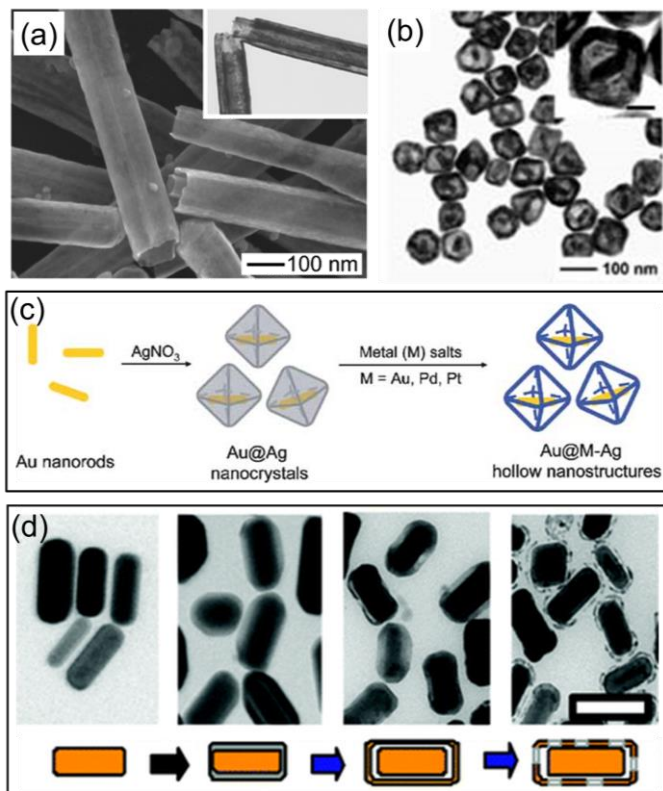


Figure 1.10 (a) SEM and TEM (inset) images of AuAg alloy double-walled nanotubes. (from Ref. [20], Sun, Y.; Wiley, B.; Li, Z.-Y.; Xia, Y. *J. Am. Chem. Soc.* **2004**, *126*, 9399.) (b) TEM image of Au-based hollow octahedral shaped rattle nanostructures with Au NRs and (c) Schematic illustration of the procedure for preparing (b). (from Ref. [21], Cho, E. C.; Camargo, P. H. C.; Xia, Y. *Adv. Mater.* **2010**, *22*, 744.) (d) TEM and schematic images of the growth of gold nanorattles. (from Ref. [22], Khalavka, Y.; Becker, J.; Sönnichsen, C. *J. Am. Chem. Soc.* **2009**, *131*, 1871.)

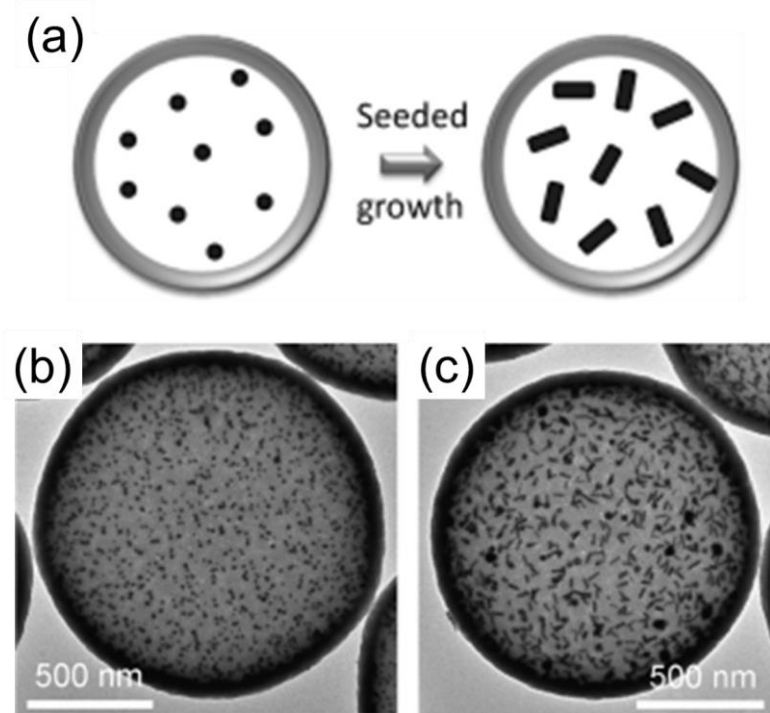


Figure 1.11 (a) An illustration of the *in situ* confined growth of Au NRs from Au nanosphere seeds inside hollow mesoporous silica shells. (b, c) TEM images showing hollow mesoporous silica shells containing Au (b) nanospheres and (c) NRs. (from Ref. [23], Goebl, J.; Yin, Y. *ChemCatChem* **2013**, 5, 1287.)

1.4 Characterization of Multi-component Metallic Nanomaterials

1.4.1 Transmission Electron Microscopy (TEM)

Transmission electron microscopy (TEM) is one of the most powerful tools to give detailed information about the size, shape, and distribution of the nanocrystal population since TEM displays a real image of the NPs. Today, thanks to the improvement in the high-voltage electron beam technique, the resolution of TEM is down to the Angstrom level which enables information to be obtained on the crystallography of the NPs. In this regard, TEM is a useful tool for characterization of multi-component nanomaterials because the particle size, morphology and lattice fringes of multi-component nanomaterials can be confirmed by TEM observation. Furthermore, the difference in electron density of two or more species provides sufficient contrast to identify their structural characteristics.

Mirkin *et al.* reported the synthesis of Au-Ag composite nanoparticles with core-shell structure.^[24] It was demonstrated that TEM analysis provided detailed information on the size, shape and structure of the hybrid nanomaterials (Figure 1.12a). The Li group showed the

crystallographic plane of Pd-Cu alloy NPs by high-resolution TEM (HR-TEM) investigation.^[25] It was revealed that the lattice fringes had an interplanar distance of 0.217 nm, is between the characteristics of face centered cubic Pd and a Cu crystal phase in the (111) plane, indicating the formation of Pd-Cu alloys (Figure 1.12b).

1.4.2 Scanning Transmission Electron Microscopy (STEM)

Another operation mode of TEM is scanning transmission electron microscopy (STEM) in which a focused electron beam is scanned across a specimen. A key difference between STEM and TEM image is the illumination used for obtaining the image. The annular dark field image available on the STEM shows nearly perfect incoherent imaging, whereas the bright field image obtained by a conventional TEM represents nearly perfect coherent imaging. When mostly incoherently scattered electrons are used to form the image, a much clearer contrast can be obtained. Therefore, combined with a high-angle annular dark-field scanning (HAADF) detector, HAADF-STEM is particularly useful for characterizing the internal structure of the multi-component nanomaterials because HAADF images are formed by collecting high-angle scattered electrons with an ADF detector and the brightness is

strongly related to the average atomic number of the scattered electrons encountered by the incident probe. For this reason, STEM is useful to measure the core-shell structures or heterostructures constituted by two elements with different atomic numbers.^[7]

Li and coworkers showed the structural arrangement of Au@Ag heterogeneous nanorods using STEM analysis.^[26] Figure 1.13a indicates that an electron density image of the Au center is brighter than that of the Ag ends of the nanorods because the different electron density of Au and Ag atoms provides sufficient contrast to distinguish the Au and the Ag. Wang *et al.* also utilized HAADF-STEM technique to analyze the relative position of the elements of AuAg/C@SiO₂ core-shell nanoparticles (Figure 1.13b).^[27] The contrast clearly shows because atomic number of Au and Ag is higher than that of SiO₂.

1.4.3 Energy Dispersive X-ray Spectroscopy (EDS)

The elemental and structural analysis of multi-component nanomaterials are investigated by various X-ray methods, such as energy-disperse X-ray spectroscopy (EDX, EDAX, or EDS), X-ray diffraction (XRD) and X-ray photoelectron spectroscopy (XPS). Owing to the characteristic binding energies of the atomic core electrons, these

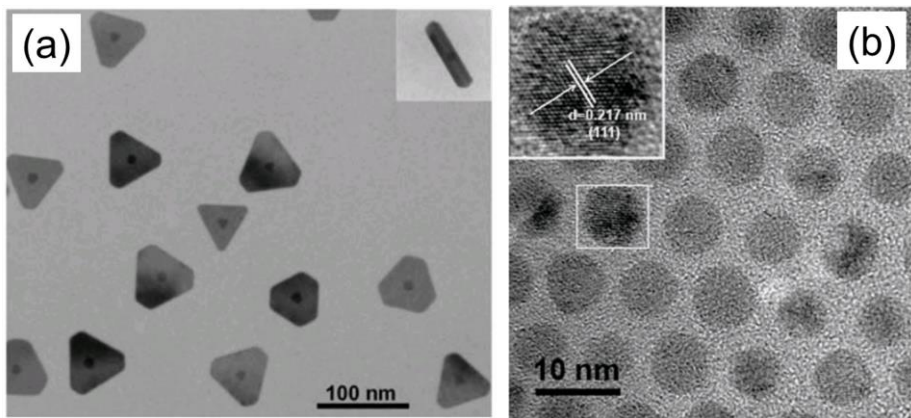


Figure 1.12 (a) TEM images of Au@Ag core-shell nanoprisms (inset: the side view of a core-shell nanoprism) (from Ref. [24], Xue, C.; Millstone, J. E.; Li, S.; Mirkin, C. A. *Angew. Chem.* **2007**, *119*, 8588.) and (b) HR-TEM image of Pd-Cu nanocrystals (from Ref. [25], Mao, J.; Liu, Y.; Chen, Z.; Wang, D.; Li, Y. *Chem. Commun.* **2014**, *50*, 4588.).

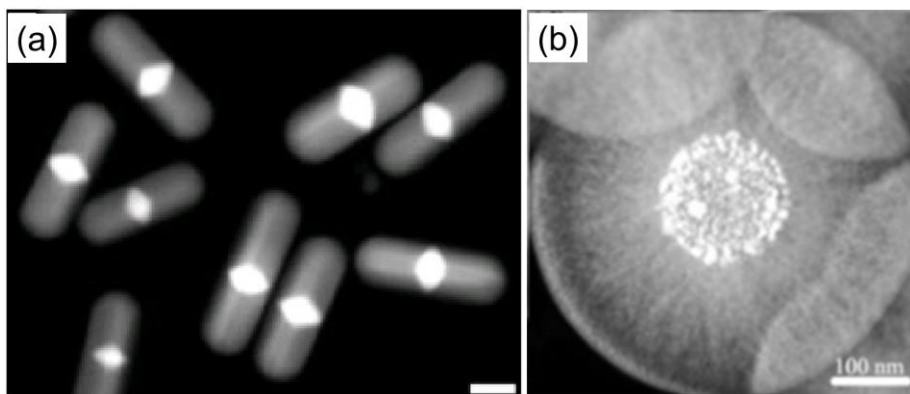


Figure 1.13 HAADF-STEM images of (a) Au@Ag heterogeneous nanorods (from Ref. [26], Li, C.; Sun, L.; Sun, Y.; Teranishi, T. *Chem. Mater.* **2013**, *25*, 2580.) and (b) AuAg/C@SiO₂ core-shell nanoparticles (from Ref. [27], Chen, Y.; Wang, Q.; Wang, T. *Dalton Trans.* **2013**, *42*, 13940.).

methods generally allow two or more metals to be distinguished. Amongst X-ray methods, EDX can be employed to elucidate the chemical composition and the elemental distribution of multi-component nanomaterials. This analytical technique is generally used in conjunction with STEM. When an electron beam strikes the surface of a sample, the X-rays are emitted with specific energies.^[28] Since their energy value and intensity depend on the material and the concentration of each element in a multi-component NP respectively, this method provides information about the regional composition and the structure of multi-component NPs.

Zhai and Song *et al.* utilized the EDX technique to elucidate the compositional distribution of Au@SiO₂@Ag@SiO₂ core-triple shell nanostructures.^[29] In spite of the large difference in electron density of Au, Ag, and SiO₂, it is hard to thoroughly observe the core-triple shell structured Au@SiO₂@Ag@SiO₂ by TEM, due to the ultrathin SiO₂ layer. Thus, they employed the EDX analysis from HAADF-STEM imaging to reveal the core-triple shell nanostructures (Figure 1.14). Au elements are marked with green color, Ag components are marked with yellow color, and SiO₂ is marked with orange color, which directly confirms the Au@SiO₂@Ag@SiO₂ core-triple shell structure.

1.4.4 X-ray diffraction (XRD)

XRD has been widely used to study the structure, crystallinity, lattice spacing, qualitative chemical composition, and particle size of multi-component nanomaterials, in particular bimetallic NPs. When an X-ray beam is incident upon a specimen, the interaction between the incident beam and the crystalline atoms causes a characteristic diffraction depending on the wavelength of X-ray irradiation and the structure of the crystal. For core-shell or heterostructure compounds, the diffraction pattern consists of overlapping peaks of the two individual monometallic NPs; while for alloyed structures, diffraction peaks of individual metals disappear and a new set of peaks corresponding to the new compound emerge.^[30]

Li *et al.* explored Pt-Cu alloy nanocrystals with different structures and their formation mechanism by XRD analysis.^[31] The XRD patterns collected at different stages during the reaction were shown in Figure 1.15. Pt/Cu-rhombic dodecahedron nanocrystals, formed at the early stage of the reaction, have the diffraction peaks near the standard reference of Cu₃Pt. Meanwhile, the XRD pattern of Pt/Cu-hexapod concave nanocrystals, the final product, is changed to the standard

reference of Cu₃Pt, which revealed that the structures and components of the alloy nanocrystals were transformed from Cu₃Pt to CuPt and the Cu content in Pt/Cu alloy decreases during the process.

1.4.5 X-ray photoelectron spectroscopy (XPS)

X-ray photoelectron spectroscopy (XPS) is informative for investigating the oxidation state and chemical composition at the surface layer of bimetallic NPs. The principle of XPS is based on analyzing the kinetic energy of the surface electrons that are excited by a monochromatic beam of X-rays. These ejected photoelectrons can be ionized from valence or core electrons of excited atoms and the core electron binding energies are characteristic of each element. Thus, the binding energies of core electrons are related to the oxidation and chemical state. Furthermore, the different photoelectron intensities of the elements can be used to determine the chemical composition because of their linear relationship with the concentration of excited atoms on the surface.^[32]

Chang's group reported the synthesis of binary hybrid nanomaterials composed of Pd and Cu.^[33] In this study, they investigated the metal-metal interaction by comparing the XPS spectra with their single

domains. As shown in Figure 1.16, the binding energies of Pd and Cu in hybrid nanoparticles were slightly shifted compared to those of pure metallic Pd NPs and Cu NPs. The shifts are ascribed to the atomic interdiffusion between Pd and Cu, revealing the formation of nanoalloys. Furthermore, the absence of the characteristic peaks of copper oxidation demonstrated that PdCu alloy NPs existed entirely in the metallic phase.

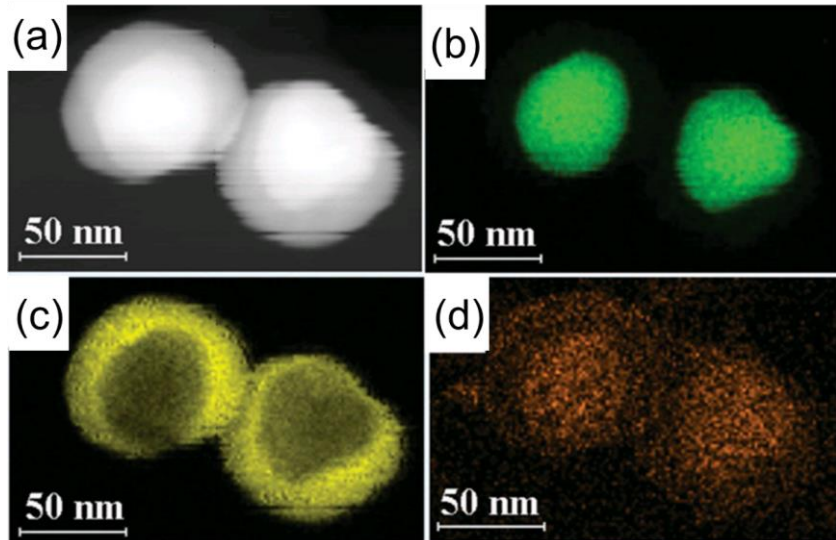


Figure 1.14 (a) HAADF-STEM image and (b-d) EDS mapping images of $\text{Au}@\text{SiO}_2@\text{Ag}@\text{SiO}_2$ nanoparticles, including (b) Au core: green; (c) Ag shell: yellow; and (d) double SiO_2 shells: orange. (from Ref. [29], Wang, Y.; Zhai, J.; Song, Y.; Lin, J.; Yin, P.; Guo, L. *Adv. Mater. Interfaces* **2015**, 2, 1500383.)

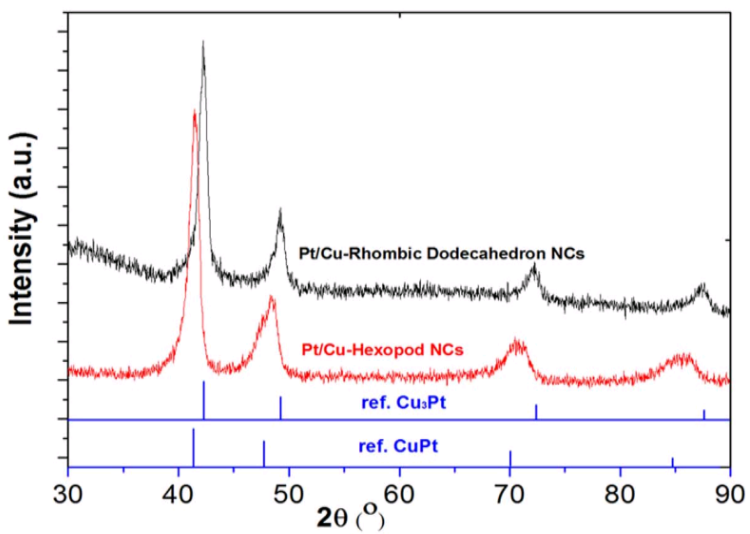


Figure 1.15 XRD patterns of PtCu rhombic dodecahedron and hexapod concave nanocrystals. (from Ref. [31], Liu, X.; Wang, W.; Li, H.; Li, L.; Zhou, G.; Yu, R.; Wang, D.; Li, Y. *Sci. Rep.* **2013**, *3*, 1404.)

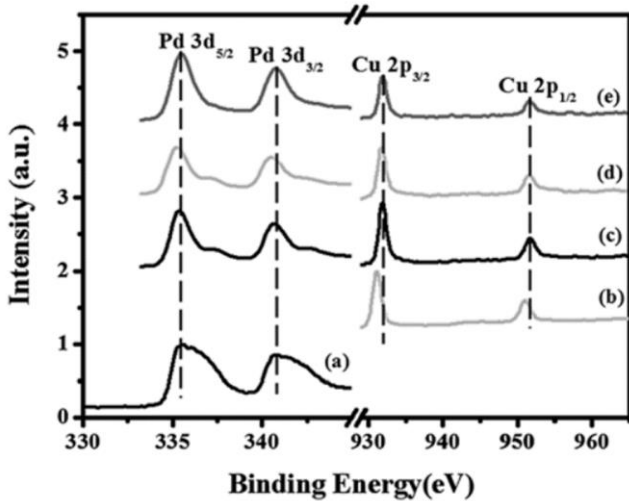


Figure 1.16 XPS spectra of (a) Pd NPs, (b) Cu NPs, and (c-e) PdCu nanoparticles prepared in the different concentration of sodium dodecyl sulfate: (c) 12.5, (d) 25, and (e) 37.5 mM. (from Ref. [33], Wu, W.-P.; Periasamy, A. P.; Lin, G.-L.; Shih, Z.-Y.; Chang, H.-T. *J. Mater. Chem. A* **2015**, *3*, 9675.)

1.5 Dissertation Overview

For many future technological applications, the development of nanomaterials with multiple components and complex structures is of paramount importance, because the electrical, optical, catalytic, and synergistic properties are strongly dependent on their compositions and structures. For this reason, intensive research has been carried out to design multi-component nanomaterials with advanced properties and develop efficient synthetic methods. My thesis focuses on the facile and controllable synthesis of multi-component metallic nanomaterials, particularly metal-metal and metal-silica systems. The synthesis method of the former is based on a solventless approach using thermal decomposition of salt powder mixed with two metal precursor solutions, while that of the latter is based on a colloidal synthetic procedure using the hard template method.

This dissertation is composed of two parts. The first part (Chapter 2) reports on the facile controlled synthesis of Ag-Cu core-shell and alloy bimetallic NPs by a solventless mix-bake-wash method. Small bimetallic nanomaterials were prepared by a one-step heating process using salt powder as a template. The particle structure could be controlled by

tuning the annealing temperature to generate hetero-structured core-shell NPs or homogeneous alloys. The NPs' bimetallic structure and elemental composition were characterized by HR-TEM, FE-SEM, EDX, HADDF-STEM, XRD and XPS. While the as-synthesized Ag@Cu core-shell NPs consist of a core of face-centered cubic (fcc) polycrystalline Ag NPs and a shell of fcc Cu including trace amounts of copper oxides, the AgCu nanoalloy was found to comprise of a single-phase NP with the same crystal structure as that of Ag, without the copper oxide species. The chemical identification of the surface species and their stability to oxidation were also confirmed by cyclic voltammetry.

The second part (Chapter 3) describes the synthesis of a highly monodisperse rattle structured nanomaterial with gold nanorods encapsulated in mesoporous silica nanocapsules (AuNR@mSiO₂) by a selective interlayer-etching process. Uniform-sized Au NRs were encapsulated inside a silver nanoshell, followed by SiO₂ coating through the sol-gel technique. After selectively etching away the silver interlayer, a rattle-structured nanomaterial was obtained. The AuNR@mSiO₂ rattle structured nanomaterials were highly uniform and well dispersed in aqueous solution. Both the hollow space and the thickness of the mesoporous silica shell were easily controlled by changing the concentration of precursor solutions.

The drug-loading efficiency was studied using the material as a drug carrier and the regrowth control of the core nanoparticles were also explored.

References

- [1] a) Huang, X.; Neretina, S.; El-Sayed, M. A. *Adv. Mater.* **2009**, *21*, 4880. b) Park, J.; Joo, J.; Kwon, S. G.; Jang, Y.; Hyeon, T. *Angew. Chem. Int. Ed.* **2007**, *46*, 4630.
- [2] a) Dreaden, E. C.; Alkilany, A. M.; Huang, X.; Murphy, C. J.; El-Sayed, M. A. *Chem. Soc. Rev.* **2012**, *41*, 2740. b) Collins, G.; Schmidt, M.; O'Dwyer, C.; Holmes, J. D.; McGlacken, G. P. *Angew. Chem. Int. Ed.* **2014**, *53*, 4142. c) Eustis, S.; El-Sayed, M. A. *Chem. Soc. Rev.* **2006**, *35*, 209. d) Linic, S.; Christopher, P.; Ingram, D. B. *Nat. Mater.* **2011**, *10*, 911.
- [3] a) Li, N.; Zhao, P.; Astruc, D. *Angew. Chem. Int. Ed.* **2014**, *53*, 1756. b) Guo, S.; Wang, E. *Nano Today* **2011**, *6*, 240. c) Jain, P. K.; Huang, X.; El-Sayed, I. H.; El-Sayed, M. A. *Acc. Chem. Res.* **2008**, *41*, 1578. d) Huang, X.; El-Sayed, I. H.; Qian, W.; El-Sayed, M. A. *J. Am. Chem. Soc.* **2006**, *128*, 2115.
- [4] a) Zhang, Q.; Lee, I.; Joo, J. B.; Zaera, F.; Yin, Y. *Acc. Chem. Res.* **2013**, *46*, 1816. b) Ghosh Chaudhuri, R.; Paria, S. *Chem. Rev.* **2012**, *112*, 2373. c) Mahmoud, M. A.; O'Neil, D.; El-Sayed, M. A. *Chem. Mater.* **2014**, *26*, 44. d) Lou, X. W.; Archer, L. A.; Yang, Z. *Adv.*

- Mater.* **2008**, *20*, 3987. e) Liu, J.; Qiao, S. Z.; Chen, J. S.; Lou, X. W.; Xing, X.; Lu, G. Q. *Chem. Commun.* **2011**, *47*, 12578. f) Pérez-Lorenzo, M.; Vaz, B.; Salgueiriño, V.; Correa-Duarte, M. A. *Chem. Eur. J.* **2013**, *19*, 12196. g) Purbia, R.; Paria, S. *Nanoscale* **2015**, *7*, 19789. h) Zhang, Q.; Wang, W.; Goebel, J.; Yin, Y. *Nano Today* **2009**, *4*, 494. i) Walther, A.; Müller, A. H. E. *Chem. Rev.* **2013**, *113*, 5194. j) Xu, Y.; Chen, L.; Wang, X.; Yao, W.; Zhang, Q. *Nanoscale* **2015**, *7*, 10559. k) Zaleska-Medynska, A.; Marchelek, M.; Diak, M.; Grabowska, E. *Adv. Colloid Interface Sci.* **2016**, *229*, 80. l) Erwin, S. C.; Zu, L.; Haftel, M. I.; Efros, A. L.; Kennedy, T. A.; Norris, D. J. *Nature* **2005**, *436*, 91. m) Maiti, U. N.; Lee, W. J.; Lee, J. M.; Oh, Y.; Kim, J. Y.; Kim, J. E.; Shim, J.; Han, T. H.; Kim, S. O. *Adv. Mater.* **2014**, *26*, 40.
- [5] Zhang, Z.; Wang, L.; Wang, J.; Jiang, X.; Li, X.; Hu, Z.; Ji, Y.; Wu, X.; Chen, C. *Adv. Mater.* **2012**, *24*, 1418.
- [6] Wang, D.; Li, Y. *Adv. Mater.* **2011**, *23*, 1044.
- [7] Ferrando, R.; Jellinek, J.; Johnston, R. L. *Chem. Rev.* **2008**, *108*, 845.
- [8] a) Schierhorn, M.; Lee, S. J.; Boettcher, S. W.; Stucky, G. D.; Moskovits, M. *Adv. Mater.* **2006**, *18*, 2829. b) Chen, Y.-S.; Frey, W.; Kim, S.; Kruizinga, P.; Homan, K.; Emelianov, S. *Nano Lett.* **2011**,

- II*, 348. c) Lee, J.; Park, J. C.; Song, H. *Adv. Mater.* **2008**, *20*, 1523.
- [9] Jankiewicz, B. J.; Jamiola, D.; Choma, J.; Jaroniec, M. *Adv. Colloid Interface Sci.* **2012**, *170*, 28.
- [10] a) Priebe, M.; Fromm, K. M. *Chem. Eur. J.* **2015**, *21*, 3854. b) Hu, S.-H.; Gao, X. *J. Am. Chem. Soc.* **2010**, *132*, 7234. c) Chen, Z.; Cui, Z.-M.; Li, P.; Cao, C.-Y.; Hong, Y.-L.; Wu, Z.-y.; Song, W.-G. *J. Phys. Chem. C* **2012**, *116*, 14986.
- [11] Wang, C.; Peng, S.; Chan, R.; Sun, S. *Small* **2009**, *5*, 567.
- [12] Liu, J.-H.; Wang, A.-Q.; Chi, Y.-S.; Lin, H.-P.; Mou, C.-Y. *J. Phys. Chem. B* **2005**, *109*, 40.
- [13] a) Jin, M.; He, G.; Zhang, H.; Zeng, J.; Xie, Z.; Xia, Y. *Angew. Chem. Int. Ed.* **2011**, *50*, 10560. b) Liu, T.; Liu, H.; Fu, C.; Li, L.; Chen, D.; Zhang, Y.; Tang, F. *J. Colloid Interface Sci.* **2013**, *400*, 168.
- [14] a) Qiang, L.; Meng, X.; Li, L.; Chen, D.; Ren, X.; Liu, H.; Ren, J.; Fu, C.; Liu, T.; Gao, F.; Zhang, Y.; Tang, F. *Chem. Commun.* **2013**, *49*, 7902. b) Yang, J.; Shen, D.; Zhou, L.; Li, W.; Li, X.; Yao, C.; Wang, R.; El-Toni, A. M.; Zhang, F.; Zhao, D. *Chem. Mater.* **2013**, *25*, 3030. c) Zhang, W.; Wang, Y.; Sun, X.; Wang, W.; Chen, L. *Nanoscale* **2014**, *6*, 14514. d) Chen, H.; Qi, B.; Moore, T.; Wang, F.; Colvin, D. C.; Sanjeeva, L. D.; Gore, J. C.; Hwu, S.-J.; Mefford, O.

- T.; Alexis, F.; Anker, J. N. *Small* **2014**, *10*, 3364. e) Huang, C.-M.; Cheng, S.-H.; Jeng, U.-S.; Yang, C.-S.; Lo, L.-W. *Nano Res.* **2012**, *5*, 654.
- [15] Bondi, J. F.; Misra, R.; Ke, X.; Sines, I. T.; Schiffer, P.; Schaak, R. E. *Chem. Mater.* **2010**, *22*, 3988.
- [16] Lee, Y. W.; Kim, M.; Kang, S. W.; Han, S. W. *Angew. Chem. Int. Ed.* **2011**, *50*, 3466.
- [17] Robinson, I.; Zacchini, S.; Tung, L. D.; Maenosono, S.; Thanh, N. T. *Chem. Mater.* **2009**, *21*, 3021.
- [18] Li, D.; Poudyal, N.; Nandwana, V.; Jin, Z.; Elkins, K.; Liu, J. P. J. *Appl. Phys.* **2006**, *99*, 08E911.
- [19] Zhang, L.; Wang, T.; Yang, L.; Liu, C.; Wang, C.; Liu, H.; Wang, Y. A.; Su, Z. *Chem. Eur. J.* **2012**, *18*, 12512.
- [20] Sun, Y.; Wiley, B.; Li, Z.-Y.; Xia, Y. *J. Am. Chem. Soc.* **2004**, *126*, 9399.
- [21] Cho, E. C.; Camargo, P. H. C.; Xia, Y. *Adv. Mater.* **2010**, *22*, 744.
- [22] Khalavka, Y.; Becker, J.; Sönnichsen, C. *J. Am. Chem. Soc.* **2009**, *131*, 1871.
- [23] Goebel, J.; Yin, Y. *ChemCatChem* **2013**, *5*, 1287.
- [24] Xue, C.; Millstone, J. E.; Li, S.; Mirkin, C. A. *Angew. Chem.* **2007**,

119, 8588.

- [25] Mao, J.; Liu, Y.; Chen, Z.; Wang, D.; Li, Y. *Chem. Commun.* **2014**, *50*, 4588.
- [26] Li, C.; Sun, L.; Sun, Y.; Teranishi, T. *Chem. Mater.* **2013**, *25*, 2580.
- [27] Chen, Y.; Wang, Q.; Wang, T. *Dalton Trans.* **2013**, *42*, 13940.
- [28] Toshima, N.; Yonezawa, T. *New J. Chem.* **1998**, *22*, 1179.
- [29] Wang, Y.; Zhai, J.; Song, Y.; Lin, J.; Yin, P.; Guo, L. *Adv. Mater. Interfaces* **2015**, *2*, 1500383.
- [30] Zhu, L.; Liang, K. S.; Zhang, B.; Bradley, J. S.; DePristo, A. E. *J. Catal.* **1997**, *167*, 412.
- [31] Liu, X.; Wang, W.; Li, H.; Li, L.; Zhou, G.; Yu, R.; Wang, D.; Li, Y. *Sci. Rep.* **2013**, *3*, 1404.
- [32] Liao, H.; Fisher, A.; Xu, Z. *J. Small* **2015**, *11*, 3221.
- [33] Wu, W.-P.; Periasamy, A. P.; Lin, G.-L.; Shih, Z.-Y.; Chang, H.-T. *J. Mater. Chem. A* **2015**, *3*, 9675.

Chapter 2. Synthesis of Ag-Cu Core-Shell and Alloy Nanoparticles via a Solventless Mix-Bake-Wash Approach

2.1 Introduction

Bimetallic NPs have attracted considerable attention for their potential applications in the fields of catalysis,^[1] optics,^[2] magnetism,^[3] and biology.^[4] In many cases, these NPs have not only the distinct characteristics of both component elements, but also new and unexpected properties from alloying owing to the synergistic effect.^[1e, 2d, 5] The preparation of bimetallic NPs has been intensively investigated for many years, and a variety of fabrication methods, including chemical reduction,^[6] thermal decomposition,^[7] sonochemical synthesis,^[8] electrochemical deposition,^[9] ion implantation,^[10] and microwave-assisted synthesis,^[11] have been developed. One of the goals of these various synthesis methods is to control the structure of bimetallic NPs to obtain specific structures such as core/shell, heterodimers, or alloy.^[12] The precise control of not only the structure but also chemical

composition, size, and atomic ordering of NPs is important to modern materials science because these factors can affect their physical and chemical properties.^[2d, 5, 13]

Among many bimetallic NPs, Cu-based NPs incorporated with noble metals in the form of core-shell or alloy structures have a number of advantages compared to mono-element metallic NPs, such as much higher catalytic activity,^[14] better antibacterial ability,^[15] and the application of low-cost conductive patterns for electronic devices.^[16] The preparation of Cu-based bimetallic NPs has been explored by many research groups in recent years. Park and Liu's groups fabricated raspberry-like Ag@Cu NPs via a stepwise reduction process using poly(vinylpyrrolidone) (PVP) as a stabilizer for preventing the aggregation of NPs;^[6a] Ying's group showed a seed-mediated growth approach for rod-shaped AuCu nanoalloys using oleylamine (OAm) as a capping agent for shape control.^[14c] Sun's group synthesized CuPd and CoPd NPs by co-reducing precursors in a solvent and a reducing agent of OAm and a stabilizer of trioctylphosphine (TOP).^[17] To the best of our knowledge, most synthetic systems of Cu-based NPs with core-shell or alloyed structures are based on wet chemical reactions, which produce uniform NPs with precise control of size and morphology. However,

many of these reactions have the disadvantages of multiple synthesis steps, necessary post-formation purification, and small-scale production limits.^[18]

Previously, some of the authors reported on the mix-bake-wash process for the preparation and treatment of nanomaterials.^[19] Herein, I report a structure-controllable and scalable one-pot synthesis of AgCu bimetallic NPs *via* this solventless mix-bake-wash approach. Small-sized bimetallic nanomaterials are obtained by heat treatment, using salt powder as a template. Moreover, the structural morphology of core-shell *versus* alloy formation can be controlled by tuning the annealing temperature. The size, structure, elemental distribution, and surface chemical identification of Ag@Cu core-shell and AgCu alloy NPs were characterized by HR-TEM, FE-SEM, EDX, HAADF-STEM, XRD, XPS, and CV measurement.

2.2 Experimental Section

2.2.1 Chemicals

Copper (II) formate tetrahydrate ($(HCO_2)_2Cu \cdot 4H_2O$, 98%) and hexylamine ($CH_3(CH_2)_5NH_2$, 99%) were obtained from Alfa Aesar and Sigma-Aldrich, respectively. Silver nitrate ($AgNO_3$, 99.8%), xylene ($C_6H_4(CH_3)_2$, 99.5%), and sodium sulfate (Na_2SO_4 , 98.5%) were purchased from Samchun Pure Chemical Co. Ltd, Korea. The sodium sulfate was processed by a grinder to obtain a homogeneous fine powder.

2.2.2 Synthesis of Ag@Cu core-shell NPs

In a typical synthesis, 0.675 g of copper (II) formate tetrahydrate (3 mmol) and 0.17 g of silver nitrate (1 mmol) were dissolved in 9 mL and 3 mL of a mixture of hexylamine/xylene (1:5 v/v), respectively. The two precursor solutions were mixed until homogeneous, and then mixed with 80 g of sodium sulfate fine powder using a mortar and pestle. The resulting powder was placed in a tube furnace with a temperature ramp of $3\text{ }^{\circ}\text{C min}^{-1}$ to $300\text{ }^{\circ}\text{C}$ under N_2 atmosphere and kept at $300\text{ }^{\circ}\text{C}$ for 1 h. After cooling to room temperature, the product was purified with 0.1 M aqueous hydrazine solution at least five times to remove salts, and then

redispersed in ethanol.

2.2.3 Synthesis of AgCu alloy NPs

The synthesis of AgCu homogeneous alloy NPs was achieved by the same procedure. In order to obtain homogeneous alloy NPs, a higher temperature was required. The annealing temperature was increased to 400 °C instead of 300 °C.

2.2.4 Physicochemical characterization

The as-prepared AgCu bimetallic NPs were characterized by low- and high-resolution (HR) transmission electron microscopy (TEM) using a JEOL JEM-2100F instrument at an acceleration voltage of 200 kV, equipped with an energy-dispersive X-ray spectroscopy (EDX) detector. EDX spectra from a bimetallic NP were taken in high-angle annular dark-field scanning transmission electron microscopy (HAADF-STEM) mode. TEM samples were prepared by drop-casting the ethanolic suspension of the NPs onto a C-coated Ni grid and air-drying. Field-emission scanning electron microscopy (FE-SEM) imaging was carried out using a Hitachi S-4800 microscope with an accelerating voltage of 15 kV. X-ray diffraction (XRD) patterns were obtained with a Bruker D8

Advanced X-ray diffractometer. X-ray photoelectron spectroscopy (XPS) investigation was conducted in a KRATOS AXIS HSi spectrometer using an Mg K α X-ray source.

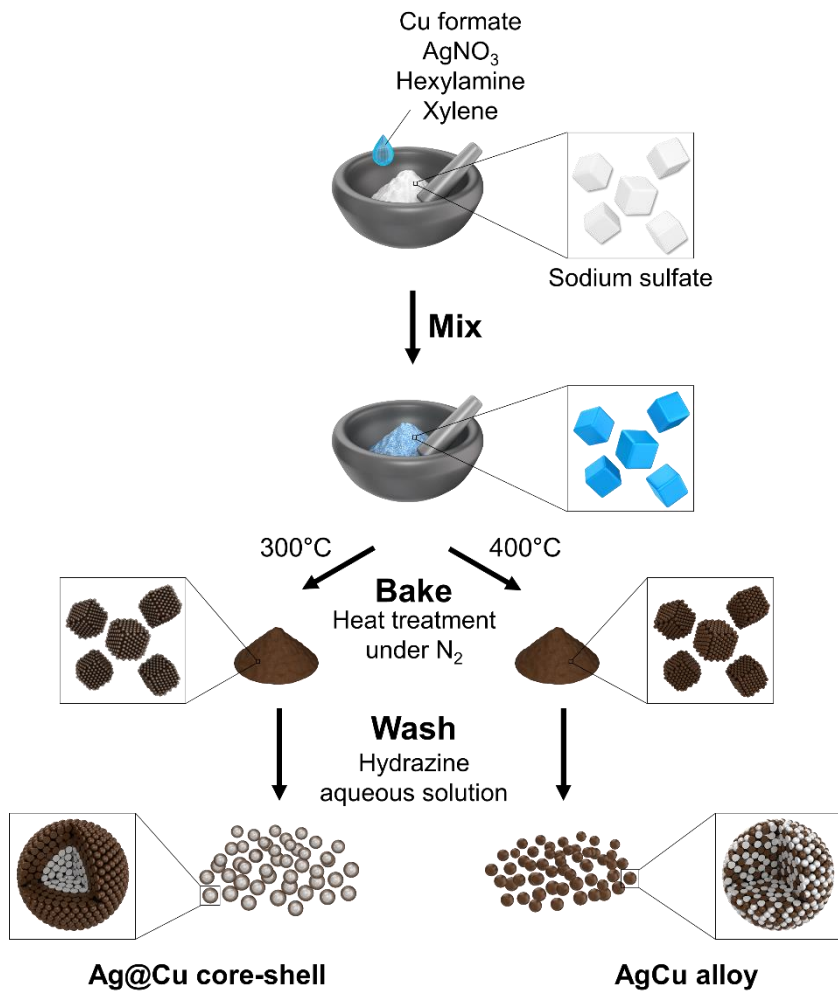
2.2.5 Electrochemical characterization

Cyclic voltammetric (CV) measurement was performed with a Metrohm Autolab PGSTAT302N Potentiostat/Galvanostat using a three-electrode electrochemical system and 0.1 M KNO₃ as the electrolyte at room temperature. A Pt wire and Hg/HgO were used as the counter electrode and the reference electrode, respectively. The working electrode was a glassy carbon electrode with a 3 mm diameter. CV curves were recorded at a scanning rate of 100 mV s⁻¹ within the potential range between -0.5 V and 0.8 V (vs. Hg/HgO).

2.3 Results and Discussion

2.3.1 Controlled synthesis of Ag-Cu core-shell and alloy bimetallic nanoparticles

Scheme 2.1 illustrates the synthetic approach for preparing Ag-Cu bimetallic NPs by the solventless mix-bake-wash method. Two types of nanostructures were synthesized: Ag@Cu hetero-structured core-shell and AgCu homogeneous alloy NPs. The first step in this synthesis was mixing salt powder with the precursor organic solution, which was prepared by dissolving Ag and Cu precursors in xylene using hexylamine as a phase transfer agent.^[20] In addition, the lone pair electrons on the nitrogen atom of hexylamine can coordinate with Ag and Cu cations to form a metal complex.^[21] After evaporation of the solvent, the mixture was heated at different temperatures to control the resulting NPs' structure under an inert N₂ atmosphere. When the reaction temperature was held at 150 °C, the initial blue color of the powder mixture began to change to red-brown, implying the formation of Cu NPs.^[22] As the reaction temperature increased, the powder turned black-brown, suggesting a bimetallic complex between the Ag and Cu NPs (Figure 2.1).^[23] SEM image of as-prepared NPs before removing the salt powder



Scheme 2.1 Schematic of the procedure for preparing Ag-Cu NPs with different bimetallic nanostructures.

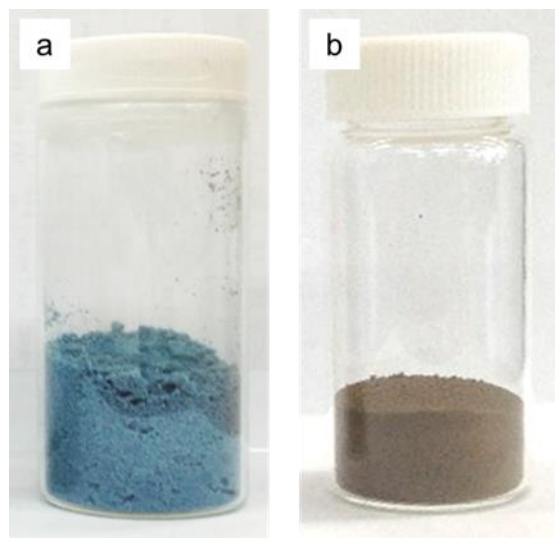


Figure 2.1 Digital photographs of (a) sodium sulfate powder mixed with Ag and Cu precursor solutions and ground by a mortar and pestle and (b) the powder after heat treatment at 400 °C.

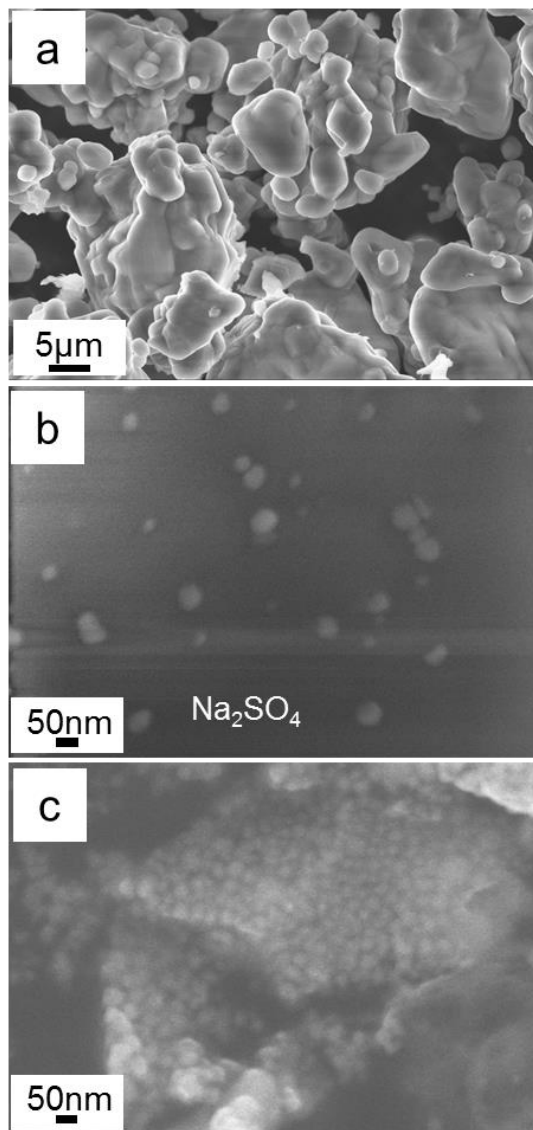


Figure 2.2 SEM images of (a) sodium sulfate powder, (b) Ag-Cu bimetallic NPs on sodium sulfate powder, and (c) Ag-Cu bimetallic NPs after removal of sodium sulfate salt powder.

showed that they were formed on the surface of the salt particles, which confirms that the salt particles function as a template for the small-sized NPs (Figure 2.2). In the final step, the synthesized NPs were obtained by washing and dissolving the salt powder in hydrazine aqueous solution, which also served to prevent oxidation of Cu.^[15a, 24]

Some typical morphologies of the Ag@Cu core-shell NPs obtained are shown in Figure 2.3a and b. They often exhibit a flower-like shape; the average diameter of these NPs is 37.8 ± 8.3 nm with an average core size of 21.4 ± 5.9 nm and a shell thickness of 8.2 ± 2.1 nm. The core-shell nanostructure can be clearly distinguished in TEM and STEM images, due to the difference in electron penetration efficiency of Ag and Cu (Figure 2.3a-c and e). HAADF-STEM imaging, in particular, shows the relative position of the elements within the nanomaterials due to the atomic number (Z)-based contrast.^[25] In this case, it can be seen that the NPs are formed of faint shells on relatively brighter cores, indicating the formation of a core-shell nanostructure; that is, an Ag core ($Z_{\text{Ag}} = 47$) encircled by a Cu shell ($Z_{\text{Cu}} = 29$). Further detailed elemental and crystallographic analysis of core-shell NPs was obtained by EDX measurements, HR-TEM imaging, and fast Fourier transform (FFT) diffraction pattern observation. Figure 2.3f shows the EDX line profiles

through the center of a single Ag@Cu NP. As observed, the Ag signal is predominantly distributed in the core region, while the Cu signal is located in the outer region of the NP. A HR-TEM image of the core shows lattice fringes with d spacing of 2.35 Å and 2.03 Å, corresponding to the (111) and (200) planes of silver, respectively, revealing that the particle is polycrystalline with multiple crystal domains (Figure 2.3c).^[26] Meanwhile, the corresponding FFT diffraction pattern shows the coexistence of cuprous oxide (Cu₂O) with monometallic Cu and Ag phases (Figure 2.3d).

In the synthesis, the ratio of Ag to Cu precursors was maintained and the heating temperature was increased to 400 °C to fabricate homogeneous alloyed NPs. Figure 2.4a and b shows TEM images of AgCu alloy NPs with an average diameter of 27.7 ± 5.4 nm. Most of the particles display close to spherical morphology. HR-TEM shows a single nanostructure with a fringe spacing of 2.35 Å, corresponding to the interplanar distance of (111) planes in face-centered cubic (fcc) Ag. The corresponding FFT diffraction pattern is also consistent with fcc Ag, suggesting that the AgCu alloy NPs have a crystal structure similar to pure Ag (Figure 2.4c and d).^[26b, 27] AgCu alloy NPs also have differently oriented domains within a single NP, implying that the prepared

nanoalloys have a polycrystalline structure. To provide definitive evidence of the alloy structure of the AgCu NPs, HAADF-STEM imaging and EDX line-scanning were performed. HAADF-STEM image shows no obvious contrast change, unlike the core-shell segregation of Ag and Cu, while EDX line-scan profiles show that Ag and Cu coexist and almost completely overlap, indicating the existence of Ag and Cu within a single nanostructure and the formation of an alloy (Figure 2.4e and f).

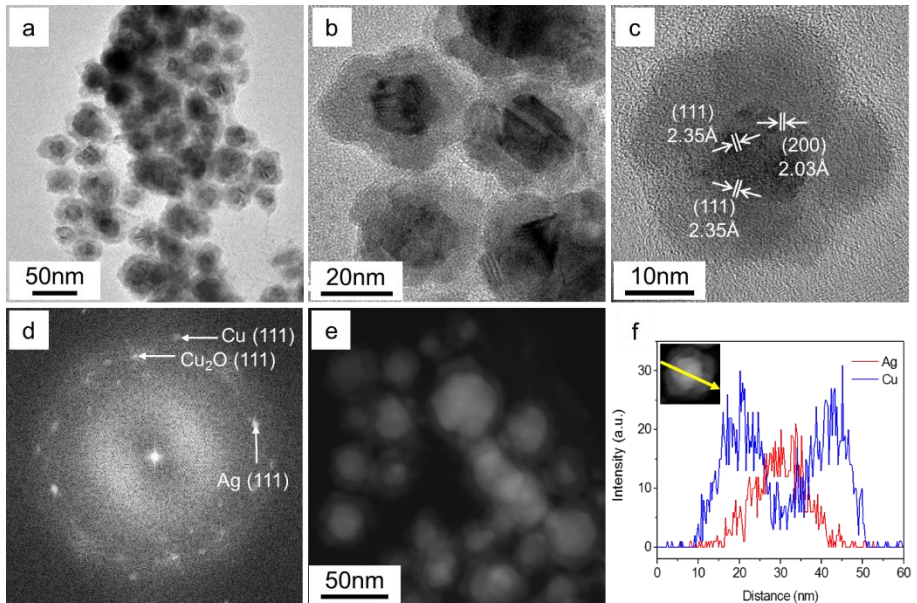


Figure 2.3 Morphological and compositional characterization of Ag@Cu core-shell NPs: (a, b) TEM images, (c) HR-TEM image, (d) FFT diffraction pattern of (c), (e) HAADF-STEM image, and (f) corresponding EDX line-scanning profiles along the line in inset.

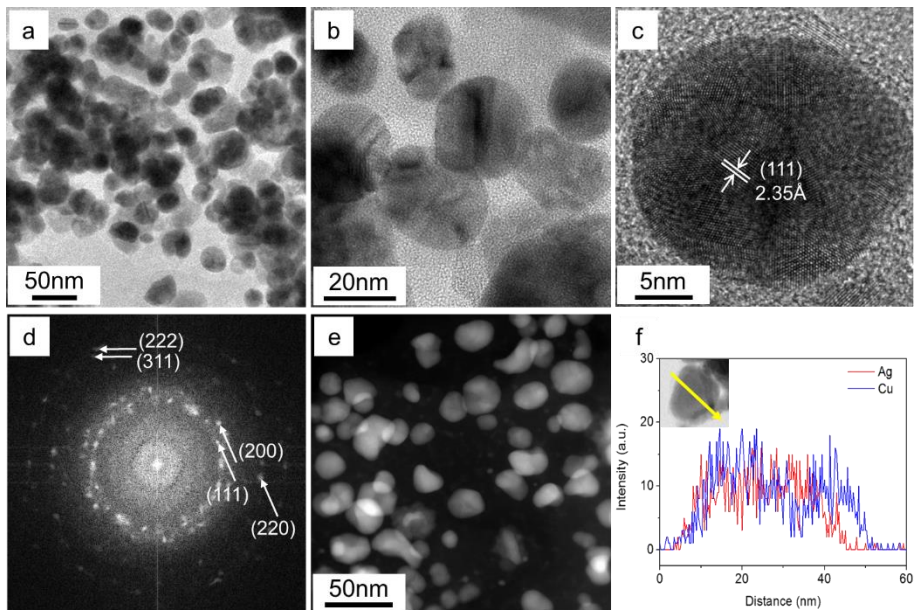


Figure 2.4 Morphological and compositional characterization of AgCu alloy NPs: (a, b) TEM images, (c) HR-TEM image, (d) FFT diffraction pattern of (c), (e) HAADF-STEM image, and (f) the corresponding EDX line-scanning profiles along the line in inset.

2.3.2 Structural and chemical characterization

The XRD patterns of bimetallic Ag@Cu core-shell and AgCu alloy NPs are shown in Figure 2.5. The diffraction peaks of the Ag@Cu core-shell NPs appear to consist of sets of peaks associated with (i) Ag (JCPDS 87-0720), (ii) Cu (JCPDS 85-1326), and (iii) copper oxides (CuO, JCPDS 80-1916; Cu₂O, JCPDS 75-1531), suggesting the segregation of Cu and Ag with fcc crystal structures and the existence of low levels of cuprous or cupric oxide, in agreement with the HR-TEM and FFT results (Figure 2.3c, d and Figure 2.5a). The XRD pattern of the AgCu alloy NPs shows four peaks at 2θ values of 38.1, 44.2, 64.4, and 77.8°. These peaks were indexed as the (111), (200), (220), and (311) planes of Ag's fcc structure, indicating that the as-prepared AgCu alloy NPs have the same crystal structure as Ag.^[15b, 28] In addition, no peaks from copper oxides were detected.

In order to further understand the formation of small-sized Ag@Cu core-shell NPs, the detailed molar ratio-dependent evolution of morphology and crystal structure were investigated by FE-SEM and XRD, as shown in Figure 2.6. When only copper (II) formate tetrahydrate was applied as a Cu precursor and heated to 300 °C, the product was large-sized spherical Cu NPs with mean diameter of about

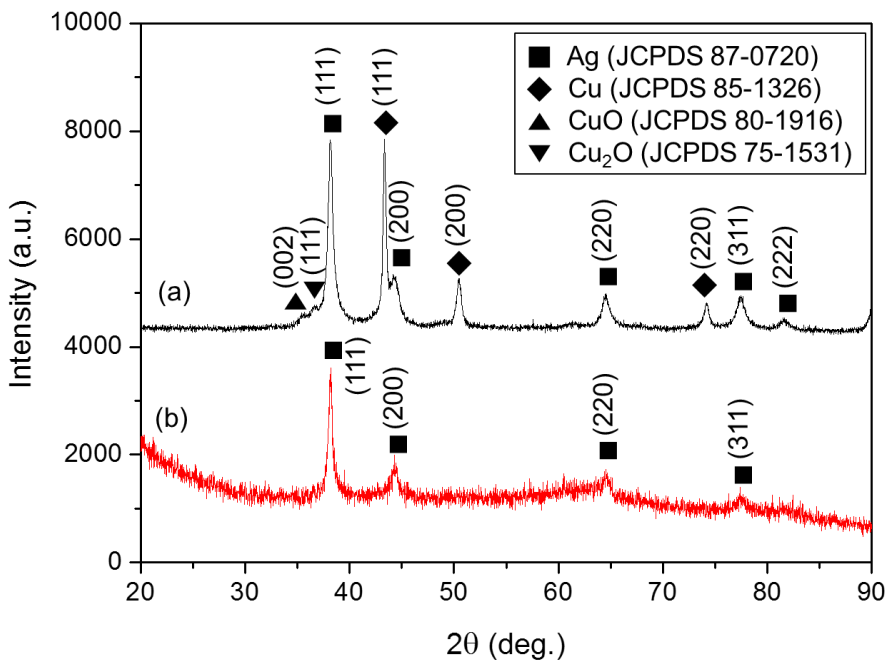


Figure 2.5 XRD patterns of the synthesized (a) Ag@Cu core-shell NPs and (b) AgCu alloy NPs. The diffraction peaks ascribed to Ag, Cu, CuO, and Cu_2O are marked with the symbols ■, ♦, ▲, and ▼, respectively.

130 nm (Figure 2.6a). These NPs had an fcc structure including trace copper oxide (Figure 2.6d). Once silver nitrate (Ag precursor) was included in the reaction mixture, a significant decrease in particle size (ca. 30-40 nm) was observed (Figure 2.6b and c). The core-shell structure can be clearly observed in Figure 2.7, and their diffraction peaks indicates the presence of both Ag and Cu, with trace copper oxides (Figure 2.6d). It was confirmed that the peak intensity of Cu increases with an increase in the molar ratio of Ag to Cu from 1:1 to 1:3, caused by a difference in the shell thickness of Cu. I observed that Ag plays an important role for the formation of small-sized Ag-Cu bimetallic NPs.

XPS was performed to further investigate the surface chemical compositions and the valence states of Cu and Ag in the Ag@Cu core-shell and AgCu alloy NPs (Figure 2.8). Figure 2.8a and c show that the Ag 3d spectra contains two sets of spin-orbit split peaks at 373.6 eV and 367.6 eV, which can be attributed to the binding energies of Ag 3d_{3/2} and Ag 3d_{5/2}, respectively. This confirms that Ag in core-shell NPs and alloy NPs exists as metallic Ag⁰.^[29] In the case of Cu in Ag@Cu core-shell NPs, as shown in Figure 2.8b, the major peaks appear at 951.6 eV for Cu 2p_{1/2} and 931.8 eV for Cu 2p_{3/2}. The Cu 2p_{3/2} peak can be further divided into two peaks at 933.8 eV and 931.7 eV, corresponding to the formation

of Cu²⁺ and Cu⁰, respectively.^[29-30] Furthermore, satellite peaks at 961.6 eV and 943.1 eV, located at higher binding energies than those of the major peaks, reveals more clearly that Ag@Cu core-shell NPs, reacted at lower temperature, contain Cu²⁺ species. However, the peak intensity of Cu²⁺ at 933.8 eV is lower than that of Cu⁰ at 931.7 eV, implying a smaller quantity of Cu²⁺ formed, compared to the amount of Cu⁰. In the case of Cu in AgCu alloy NPs, the spin-orbit split Cu peaks at 951.9 eV and 932.0 eV agree with the binding energies of Cu 2p_{1/2} and Cu 2p_{3/2} of metallic Cu⁰, respectively; no oxide species were detected.^[29-30, 31] The above information provides sufficient evidence that AgCu alloy NPs existed fully in the metallic state, whereas some Cu atoms in the Ag@Cu core-shell NPs experienced oxidation.

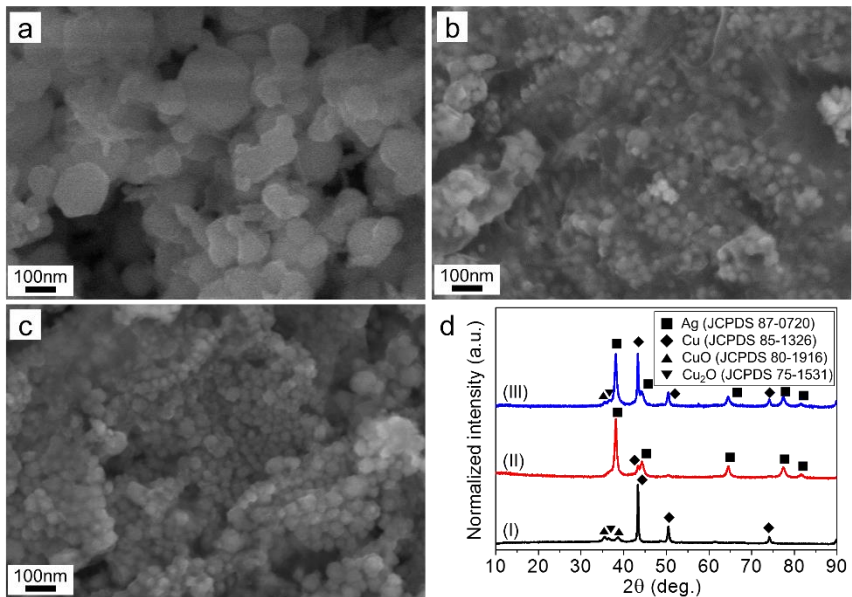


Figure 2.6 SEM and XRD patterns of pure Cu NPs (a), Ag@Cu core-shell NPs with Ag to Cu molar ratios of 1:1 (b) and 1:3 (c). (d) Comparison of XRD patterns of pure Cu (I), Ag@Cu core-shell NPs with Ag to Cu molar ratios of 1:1 (II) and 1:3 (III). The diffraction peaks ascribing to Ag, Cu, CuO, and Cu_2O are marked with the symbols ■, ♦, ▲, and ▼, respectively.

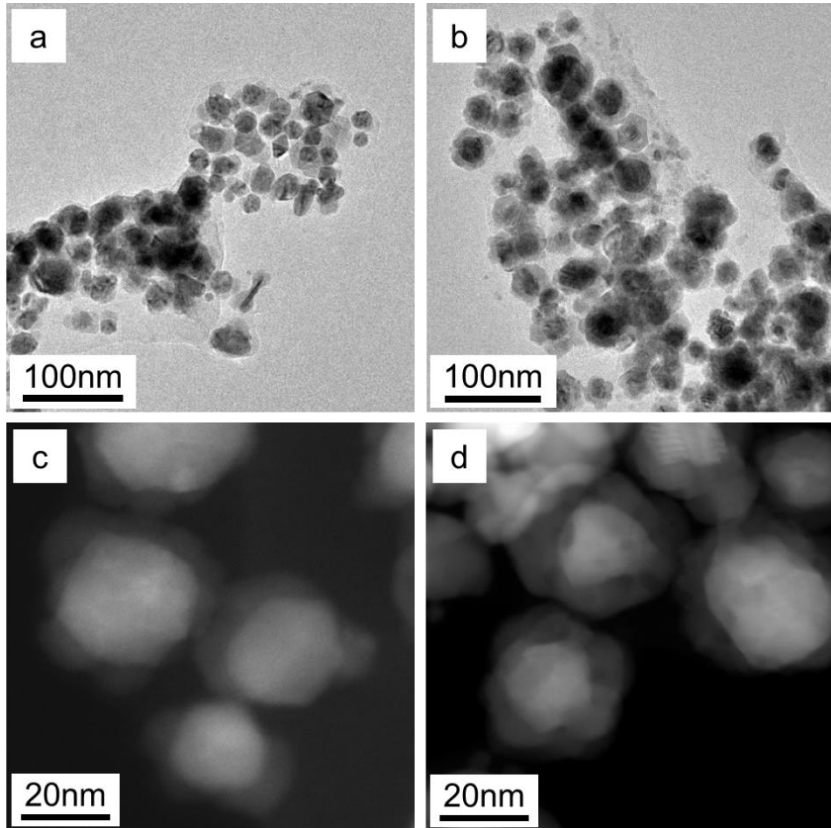


Figure 2.7 TEM and HAADF-STEM images of Ag@Cu core-shell NPs with different molar ratios of Ag to Cu; (a, c) Ag:Cu = 1:1 and (b, d) Ag:Cu = 1:3.

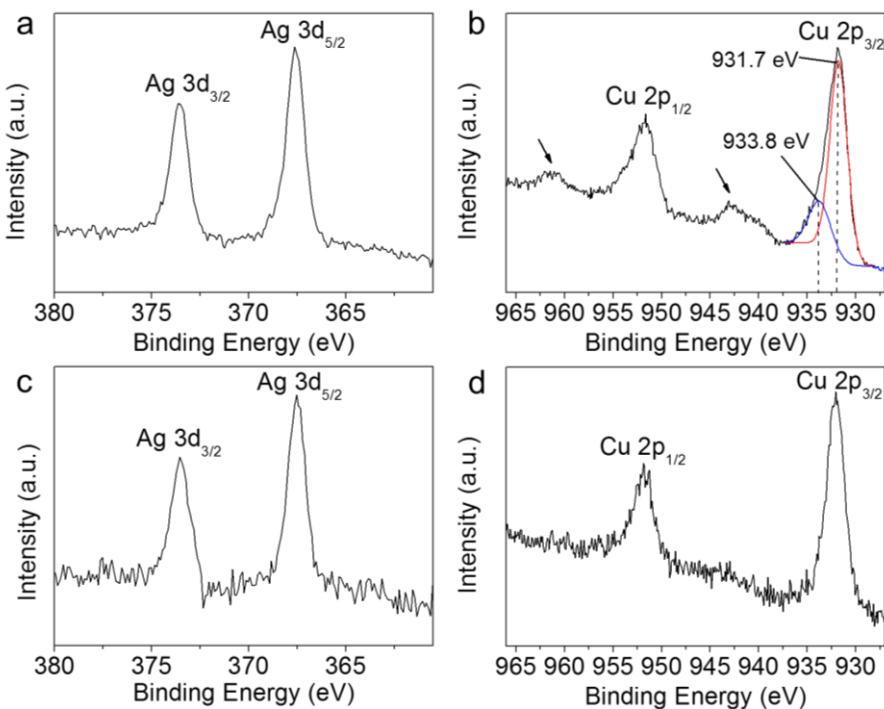


Figure 2.8 XPS patterns in the binding energy range of (a, c) Ag 3d and (b, d) Cu 2p from (a, b) Ag@Cu core-shell NPs and (c, d) AgCu alloy NPs, respectively.

2.3.3 Investigation of the effect of salt powder on the synthesis of Ag-Cu bimetallic nanoparticles

To check the ability of the solventless mix-bake-wash method to obtain small-sized uniform bimetallic NPs, an additional experiment was performed. Under similar reaction conditions but without the salt powder, additional AgCu alloy NPs were synthesized. Specifically, precursor organic solution was dropped on Si wafer and it was left at room temperature for 5 h under N₂ atmosphere in a tube furnace to evaporate the xylene completely. And then, the sample was heated up to 400 °C with a rate of 3 °C min⁻¹ and maintained for 1 h at this temperature. Instead of forming alloyed bimetallic NPs, Ag-Cu aggregates with various sizes were generated, which confirms that salt powder can act as a template to avoid aggregation and produce small-sized NPs.

As can be seen from these results, the solventless mix-bake-wash approach in this work has several advantages. First, this strategy is attractive and practical to synthesize alloy NPs because salt powder has a very wide temperature window from 200 to 600 °C. In addition, the salt powder serves as a template to prevent aggregation of NPs during synthesis, instead of capping agents in a wet chemical method. Second, the structural morphology of core-shell and alloy can be easily controlled

by tuning the annealing temperature. Lastly, the proposed synthetic strategy can be readily scalable for nanomaterial fabrication on an industrial scale.

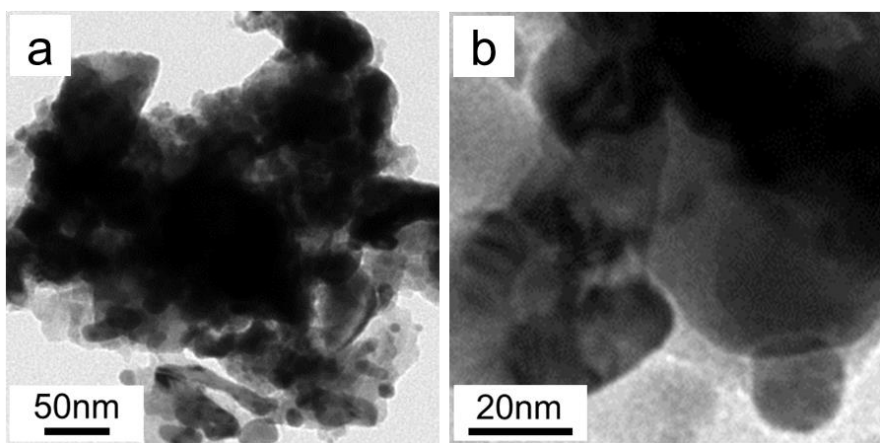


Figure 2.9 (a, b) TEM images of aggregates prepared under the same reaction conditions for AgCu alloy NPs in absence of salt powders.

2.3.4 Electrochemical analysis of Ag-Cu bimetallic nanoparticles

The surface structure of Ag-Cu bimetallic NPs is one of the key factors affecting their catalytic and electrical performance.^[16a, 32]

CV is an efficacious method to study surface reactions of metals.^[33] I conducted CV measurements to investigate the chemical identification of the surface species. Figure 2.10 shows the CV curves of Ag@Cu core-shell and AgCu alloy NPs with equal weight in 0.1 M KNO₃ at a potential range of -0.5 ~ 0.8 V vs. Hg/HgO. The typical two anodic peaks corresponding to the oxidation of Cu from Ag@Cu core-shell NPs were observed at 0.111 V and 0.239 V (vs. Hg/HgO), which can be attributed to the dissolution of Cu.^[34] For AgCu alloy NPs, there is one oxidation peak in the forward scan. The peak current, depending on both the size of NPs and the compositional and structural features of the two constituent elements, was significantly decreased as compared to that of Ag@Cu core-shell NPs.^[17] This result supports the observation that the surface of AgCu alloy NPs are composed of relatively low Cu content, in good agreement with TEM and EDX results, and the oxidation resistance is enhanced by alloying.

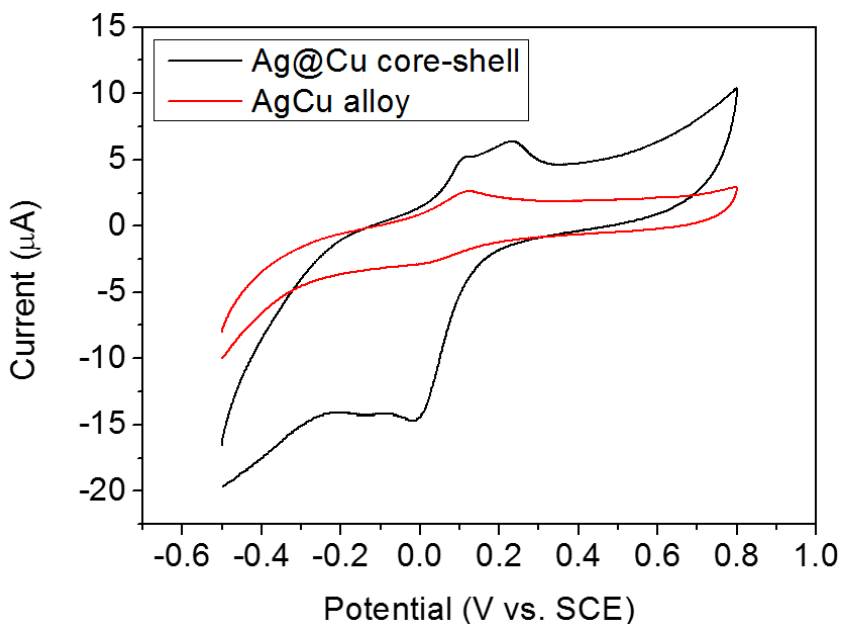


Figure 2.10 Cyclic voltammogram curves of Ag@Cu core-shell NPs (black line) and AgCu alloy NPs (red line) recorded in 0.1 M KNO_3 . Scan rate: 100 mV s^{-1} .

2.4 Conclusion

A solventless mix-bake-wash method using salt powder was developed to fabricate uniform Ag-Cu core-shell and alloy bimetallic NPs. The feature of our synthetic strategy that distinguishes it from those reported earlier is the use of salt powder, which serves as a template to prevent the aggregation of NPs during synthesis. The as-synthesized Ag-Cu bimetallic NPs have diameters in the range of 30-40 nm. The structures of the NPs can be tuned by the reaction temperature, allowing for selection between hetero-structured core-shell NPs and homogeneous alloys. Ag@Cu core-shell NPs show a flower-like shape and consist of fcc metal Ag and Cu, with trace levels of copper oxides. AgCu nanoalloys show a single phase with fcc structure similar to Ag, containing no copper oxides. The results of CV indicated that the surface of AgCu alloy NPs are composed by relatively low Cu content and the oxidation resistance is enhanced by alloying. The methodology reported here has distinct advantages: 1) the lack of solvent makes it possible to synthesize alloys in a wide temperature window. 2) The structural morphology of core-shell versus alloy can be tuned by adjusting only the annealing temperature. 3) The proposed synthesis strategy is easily

scalable for large-scale production. I believe that this approach can be extended to produce other important bimetallic NPs, such as CuAu and CuPt. These structure-controlled bimetallic NPs may have great potential for many applications related to electronics, biomedical research, and catalysis.

References

- [1] a) Wang, D.; Li, Y. *Adv. Mater.* **2011**, *23*, 1044. b) Burda, C.; Chen, X.; Narayanan, R.; El-Sayed, M. A. *Chem. Rev.* **2005**, *105*, 1025. c) Alayoglu, S.; Nilekar, A. U.; Mavrikakis, M.; Eichhorn, B. *Nat. Mater.* **2008**, *7*, 333. d) Son, S. U.; Jang, Y.; Park, J.; Na, H. B.; Park, H. M.; Yun, H. J.; Lee, J.; Hyeon, T. *J. Am. Chem. Soc.* **2004**, *126*, 5026. e) Sun, D.; Mazumder, V.; Metin, O.; Sun, S. *ACS nano* **2011**, *5*, 6458. f) Wang, D.; Peng, Q.; Li, Y. *Nano Res.* **2010**, *3*, 574.
- [2] a) Chen, O.; Zhao, J.; Chauhan, V. P.; Cui, J.; Wong, C.; Harris, D. K.; Wei, H.; Han, H.-S.; Fukumura, D.; Jain, R. K.; Bawendi, M. G. *Nat. Mater.* **2013**, *12*, 445. b) Wilcoxon, J. P.; Provencio, P. P. *J. Am. Chem. Soc.* **2004**, *126*, 6402. c) Wang, L.; Clavero, C.; Huba, Z.; Carroll, K. J.; Carpenter, E. E.; Gu, D.; Lukaszew, R. A. *Nano Lett.* **2011**, *11*, 1237. d) Ferrando, R.; Jellinek, J.; Johnston, R. L. *Chem. Rev.* **2008**, *108*, 845.
- [3] a) Bussian, D. A.; Crooker, S. A.; Yin, M.; Brynda, M.; Efros, A. L.; Klimov, V. I. *Nat. Mater.* **2008**, *8*, 35. b) Wei, X.; Zhou, R.; Lefebvre, W.; He, K.; Le Roy, D.; Skomski, R.; Li, X.; Shield, J. E.; Kramer, M. J.; Chen, S.; Zeng, X. C.; Sellmyer, D. J. *Nano Lett.* **2014**, *14*,

1362. c) Bondi, J. F.; Misra, R.; Ke, X.; Sines, I. T.; Schiffer, P.; Schaak, R. E. *Chem. Mater.* **2010**, *22*, 3988. d) Demortière, A.; Petit, C. *Langmuir* **2007**, *23*, 8575.
- [4] a) Rosi, N. L.; Mirkin, C. A. *Chem. Rev.* **2005**, *105*, 1547. b) Wang, F.; Deng, R.; Wang, J.; Wang, Q.; Han, Y.; Zhu, H.; Chen, X.; Liu, X. *Nat. Mater.* **2011**, *10*, 968. c) Nam, J.-M.; Stoeva, S. I.; Mirkin, C. A. *J. Am. Chem. Soc.* **2004**, *126*, 5932.
- [5] Kobayashi, H.; Yamauchi, M.; Kitagawa, H.; Kubota, Y.; Kato, K.; Takata, M. *J. Am. Chem. Soc.* **2010**, *132*, 5576.
- [6] a) Lee, J.-P.; Chen, D.; Li, X.; Yoo, S.; Bottomley, L. A.; El-Sayed, M. A.; Park, S.; Liu, M. *Nanoscale* **2013**, *5*, 11620. b) Andolina, C. M.; Dewar, A. C.; Smith, A. M.; Marbella, L. E.; Hartmann, M. J.; Millstone, J. E. *J. Am. Chem. Soc.* **2013**, *135*, 5266. c) Ko, W.-Y.; Su, J.-W.; Guo, C.-H.; Lin, K.-J. *Carbon* **2012**, *50*, 2244.
- [7] a) Sun, S.; Murray, C.; Weller, D.; Folks, L.; Moser, A. *Science* **2000**, *287*, 1989. b) Hyeon, T. *Chem. Commun.* **2003**, 927. c) Kim, B. Y.; Shim, I.-B.; Araci, Z. O.; Saavedra, S. S.; Monti, O. L.; Armstrong, N. R.; Sahoo, R.; Srivastava, D. N.; Pyun, J. *J. Am. Chem. Soc.* **2010**, *132*, 3234.
- [8] a) Mizukoshi, Y.; Fujimoto, T.; Nagata, Y.; Oshima, R.; Maeda, Y. *J.*

- Phys. Chem. B* **2000**, *104*, 6028. b) Anandan, S.; Grieser, F.; Ashokkumar, M. *J. Phys. Chem. C* **2008**, *112*, 15102.
- [9] a) Song, Y.; Ma, Y.; Wang, Y.; Di, J.; Tu, Y. *Electrochim. Acta* **2010**, *55*, 4909. b) Kolb, U.; Quaiser, S. A.; Winter, M.; Reetz, M. T. *Chem. Mater.* **1996**, *8*, 1889.
- [10] a) Pena, O.; Pal, U.; Rodríguez-Fernández, L.; Silva-Pereyra, H. G.; Rodríguez-Iglesias, V.; Cheang-Wong, J. C.; Arenas-Alatorre, J.; Oliver, A. *J. Phys. Chem. C* **2009**, *113*, 2296. b) Mattei, G.; Maurizio, C.; Mazzoldi, P.; D'Acapito, F.; Battaglin, G.; Cattaruzza, E.; de Julián Fernández, C.; Sada, C. *Phys. Rev. B* **2005**, *71*, 195418.
- [11] a) Harpeness, R.; Gedanken, A. *Langmuir* **2004**, *20*, 3431. b) Liu, Z.; Lee, J. Y.; Chen, W.; Han, M.; Gan, L. M. *Langmuir* **2004**, *20*, 181.
- [12] a) Teng, X.; Yang, H. *J. Am. Chem. Soc.* **2003**, *125*, 14559. b) Nakhjavan, B.; Tahir, M. N.; Natalio, F.; Gao, H.; Schneider, K.; Schladt, T.; Ament, I.; Branscheid, R.; Weber, S.; Kolb, U.; Sonnichsen, C.; Schreiber, L. M.; Tremel, W. *J. Mater. Chem.* **2011**, *21*, 8605.
- [13] a) Tao, F.; Grass, M. E.; Zhang, Y.; Butcher, D. R.; Renzas, J. R.; Liu, Z.; Chung, J. Y.; Mun, B. S.; Salmeron, M.; Somorjai, G. A.

Science **2008**, *322*, 932. b) Yan, J.-M.; Zhang, X.-B.; Han, S.; Shioyama, H.; Xu, Q. *J. Power Sources* **2009**, *194*, 478. c) Chen, H. M.; Hsin, C. F.; Chen, P. Y.; Liu, R.-S.; Hu, S.-F.; Huang, C.-Y.; Lee, J.-F.; Jang, L.-Y. *J. Am. Chem. Soc.* **2009**, *131*, 15794. d) Shin, K.; Kim, D. H.; Lee, H. M. *ChemSusChem* **2013**, *6*, 1044.

[14] a) Sugano, Y.; Shiraishi, Y.; Tsukamoto, D.; Ichikawa, S.; Tanaka, S.; Hirai, T. *Angew. Chem.* **2013**, *125*, 5403. b) Piccinin, S.; Zafeiratos, S.; Stampfl, C.; Hansen, T. W.; Hävecker, M.; Teschner, D.; Bukhtiyarov, V. I.; Girgsdies, F.; Knop-Gericke, A.; Schlögl, R.; Scheffler, M. *Phys. Rev. Lett.* **2010**, *104*, 035503. c) Yang, J.; Chng, L. L.; Yang, X.; Chen, X.; Ying, J. Y. *Chem. Commun.* **2014**, *50*, 1141. d) Wu, W.; Lei, M.; Yang, S.; Zhou, L.; Liu, L.; Xiao, X.; Jiang, C.; Roy, V. A. L. *J. Mater. Chem. A* **2015**, *3*, 3450. e) Liu, J.; Wu, Q.; Huang, F.; Zhang, H.; Xu, S.; Huang, W.; Li, Z. *RSC Adv.* **2013**, *3*, 14312.

[15] a) Taner, M.; Sayar, N.; Yulug, I. G.; Suzer, S. *J. Mater. Chem.* **2011**, *21*, 13150. b) Valodkar, M.; Modi, S.; Pal, A.; Thakore, S. *Mater. Res. Bull.* **2011**, *46*, 384.

[16] a) Grouchko, M.; Kamyshny, A.; Magdassi, S. *J. Mater. Chem.* **2009**, *19*, 3057. b) Kim, S. J.; Stach, E. A.; Handwerker, C. A. *Appl. Phys.*

- Lett.* **2010**, *96*, 144101. c) Kim, C. K.; Lee, G.-J.; Lee, M. K.; Rhee, C. K. *Powder Technol.* **2014**, *263*, 1.
- [17] Mazumder, V.; Chi, M.; Mankin, M. N.; Liu, Y.; Metin, O. n.; Sun, D.; More, K. L.; Sun, S. *Nano Lett.* **2012**, *12*, 1102.
- [18] Yan, T.; Zhong, X.; Rider, A. E.; Lu, Y.; Furman, S. A.; Ostrikov, K. *Chem. Commun.* **2014**, *50*, 3144.
- [19] a) Jang, B.; Park, M.; Chae, O. B.; Park, S.; Kim, Y.; Oh, S. M.; Piao, Y.; Hyeon, T. *J. Am. Chem. Soc.* **2012**, *134*, 15010. b) Park, Y. I.; Piao, Y.; Lee, N.; Yoo, B.; Kim, B. H.; Choi, S. H.; Hyeon, T. *J. Mater. Chem.* **2011**, *21*, 11472. c) Piao, Y.; Kim, J.; Na, H. B.; Kim, D.; Baek, J. S.; Ko, M. K.; Lee, J. H.; Shokouhimehr, M.; Hyeon, T. *Nat. Mater.* **2008**, *7*, 242.
- [20] Liu, L.; Kelly, T. L. *Langmuir* **2013**, *29*, 7052.
- [21] a) Kim, S. J.; Lee, J.; Choi, Y.-H.; Yeon, D.-H.; Byun, Y. *Thin Solid Films* **2012**, *520*, 2731. b) Vaseem, M.; McKerricher, G.; Shamim, A. *ACS Appl. Mater. Interfaces* **2016**, *8*, 177. c) Hansen, L. D.; Temer, D. J. *Inorg. Chem.* **1971**, *10*, 1439.
- [22] Jin, M.; He, G.; Zhang, H.; Zeng, J.; Xie, Z.; Xia, Y. *Angew. Chem. Int. Ed.* **2011**, *50*, 10560.
- [23] Sra, A. K.; Schaak, R. E. *J. Am. Chem. Soc.* **2004**, *126*, 6667.

- [24] Magdassi, S.; Grouchko, M.; Kamyshny, A. *Materials* **2010**, *3*, 4626.
- [25] a) Pennycook, S. J.; Jesson, D. E. *Ultramicroscopy* **1991**, *37*, 14. b) Pennycook, S. J.; Jesson, D. E. *Acta Metall. Mater.* **1992**, *40*, S149. c) López-Ortega, A.; Estrader, M.; Salazar-Alvarez, G.; Roca, A. G.; Nogués, J. *Phys. Rep.* **2015**, *553*, 1.
- [26] a) Bai, T.; Sun, J.; Che, R.; Xu, L.; Yin, C.; Guo, Z.; Gu, N. *ACS Appl. Mater. Interfaces* **2014**, *6*, 3331. b) Chen, M.; Wang, C.; Wei, X.; Diao, G. *J. Phys. Chem. C* **2013**, *117*, 13593.
- [27] Yang, T. I.; Brown, R. N. C.; Kempel, L. C.; Kofinas, P. *Nanotechnology* **2011**, *22*, 105601.
- [28] a) Lei, Y.; Chen, F.; Huang, B.; Liu, Z. *Mater. Res. Express* **2014**, *1*, 015031. b) Huang, C.-H.; Wang, H. P.; Chang, J.-E.; Eyring, E. M. *Chem. Commun.* **2009**, 4663.
- [29] Morrish, R.; Muscat, A. J. *Chem. Mater.* **2009**, *21*, 3865.
- [30] a) Noh, H.-B.; Lee, K.-S.; Chandra, P.; Won, M.-S.; Shim, Y.-B. *Electrochim. Acta* **2012**, *61*, 36. b) Bansal, V.; Jani, H.; Du Plessis, J.; Coloe, P. J.; Bhargava, S. K. *Adv. Mater.* **2008**, *20*, 717.
- [31] a) Shin, D.-H.; Woo, S.; Yem, H.; Cha, M.; Cho, S.; Kang, M.; Jeong, S.; Kim, Y.; Kang, K.; Piao, Y. *ACS Appl. Mater. Interfaces* **2014**, *6*, 3312. b) Yin, Z.; Lee, C.; Cho, S.; Yoo, J.; Piao, Y.; Kim, Y. S. *Small*

2014, *10*, 5047.

- [32] Holewinski, A.; Idrobo, J.-C.; Linic, S. *Nat. Chem.* **2014**, *6*, 828.
- [33] a) Aljohani, T. A.; Hayden, B. E. *Electrochim. Acta* **2013**, *111*, 930.
b) Chen, D.; Jin, N.; Chen, W.; Wang, L.; Zhao, S.; Luo, D. *Surf. Coat. Technol.* **2014**, *254*, 440.
- [34] Zhang, T.; Yuan, R.; Chai, Y.; Li, W.; Ling, S. *Sensors* **2008**, *8*, 5141.

Chapter 3. Rattle Structured Nanomaterials of Gold Nanorod Encapsulated in Mesoporous Silica Nanocapsule for Drug Delivery and Nanoscaled Reaction

3.1 Introduction

Over the past two decades, hollow-structured nanomaterials have gathered increased interest owing to potential applications as nanoreactors and in nanocatalysis and the biomedical field.^[1] Recently, hollow-structured nanomaterials with a movable core, which are referred to as “rattle-structured nanomaterials,” have attracted tremendous attention because they allow the optical, electric, and magnetic properties of the core material to be added to the nanomaterial.^[2] Until recently, there have been a variety of approaches for the preparation of rattle-structured nanomaterials. Sönnichsen *et al.* reported gold nanorattles obtained through the Kirkendall effect.^[3] Further, a Au@SiO₂ core/shell nanostructure could be transferred into a rattle-shaped one by a further selective core-etching process.^[2b] In addition, a template-assisted etching

approach,^[4] the Ostwald ripening process,^[5] and a water-in-oil microemulsion method^[6] have also been used to prepare rattle-structured nanomaterials.

Of the various rattle-type mesoporous nanomaterial systems, the rattle-structured nanomaterial composed of Au NR in mesoporous silica nanocapsule is expected to attract a great deal of interest. On one hand, the mesoporous silica shell possesses the advantages of low cytotoxicity, uniform size, high stability, easy functionalization, high pore volumes, and low cost.^[7] On the other hand, Au NRs offer fascinating tuned surface plasmon resonance (SPR) properties,^[8] which make them well suited for diverse biomedical applications such as diagnosis, photothermal therapy, bio-imaging, and biological sensing.^[9] Herein, I report a novel solution-based consecutive process for the fabrication of a highly monodisperse rattle-structured nanomaterial composed of Au NRs in mesoporous silica nanocapsules. The resulting nanostructured materials were highly uniform in morphology and showed good dispersibility properties, similar to the initial Au NRs. Drug loading was studied using the material as a drug carrier and doxorubicin hydrochloride (DOX) as a model. In addition, Au NRs inside the confined mesoporous silica nanocapsules were further regrown in a

controlled manner by simply adding gold precursor and ascorbic acid (AA).

3.2 Experimental Section

3.2.1 Chemicals

Cetyltrimethylammonium bromide (CTAB, 95%), sodium borohydride (NaBH_4 , ≥98.0%), gold(III) chloride trihydrate ($\text{HAuCl}_4 \cdot 3\text{H}_2\text{O}$, ≥99.9%), silver nitrate (AgNO_3 , 99.999%), L-ascorbic acid (AA, ≥99%), and doxorubicin hydrochloride (DOX, ≥98.0%) were all obtained from Sigma-Aldrich. Sodium hydroxide (NaOH), tetraethyl orthosilicate (TEOS, 98.0%), and hydrogen peroxide (H_2O_2 , 30.0-35.5% (SG)) were purchased from Samchun. Ultrapure deionized water was used for all solution preparations and experiments.

3.2.2 Preparation of Au nanorods

Gold nanorods (AuNRs) were synthesized using a seed-mediated growth method with slight modifications according to the report by Murphy *et al.*^[10] As in a typical synthesis procedure, the seed solution was prepared by adding 600 μL of ice-cold 0.01 M NaBH_4 to an aqueous

solution containing 250 μ L of 0.01 M HAuCl₄·3H₂O and 7.5 mL of 0.1 M CTAB under vigorous stirring. The color of the solution immediately changed from yellow to brown, indicating the formation of gold nanoparticle seeds. The solution was constantly stirred for 2 h. For the growth of seeds, an aqueous growth solution containing 9.5 mL of 0.1 M CTAB, 400 μ L of 0.01 M HAuCl₄·3H₂O, 60 μ L of 0.01 M AgNO₃, and 64 μ L of 0.1 M AA was prepared. AuNRs were grown by adding 10 μ L of the seed solution to the growth solution and leaving this mixture overnight.

3.2.3 Synthesis of AuNR@Ag core/shell nanoparticles

Silver-coated AuNRs were prepared using a modified procedure proposed by Xie *et al.*^[11] 20 μ L of 0.1 M AA and 1 mL of 0.01 M AgNO₃ were mixed with 6 mL of as-prepared Au NRs. 300 μ L of 0.1 M NaOH was then added to this mixture to increase the pH to 10 because AA could reduce silver ions only in a basic medium.^[8, 12] The mixture was vigorously stirred for 2 h to ensure complete coating of silver.

3.2.4 Synthesis of AuNR@Ag@mSiO₂ core/shell/shell nanoparticles

CTAB-stabilized AuNR@Ag nanoparticles were coated with

mesoporous silica shells through the Stöber method. For this purpose, a slightly modified version of the procedure described by Matsuura *et al.* was employed.^[13] 5 mL of an as-prepared AuNR@Ag colloid solution was mixed with 25 µL of 0.1 M NaOH under stirring. Thereafter, 30 µL of TEOS dispersed in methanol (10% v/v) was added at 1 h intervals for 3 h under gentle stirring. The reaction was allowed to proceed for 24 h at room temperature.

3.2.5 Synthesis of rattle-structured AuNR@mSiO₂ core/void/shell nanoparticles

I used H₂O₂ for removing silver. Silver can be selectively etched by H₂O₂ because the standard redox potential of H₂O₂ is more positive than that of silver.^[14] Under magnetic stirring, 8 mL of H₂O₂ was added to 4 mL of a AuNR@Ag@mSiO₂ solution, and the mixture was left undisturbed for over 12 h. The obtained rattle-structured AuNR@mSiO₂ nanoparticles were then centrifuged and washed with ethanol at least twice and redispersed in ethanol (4 mL).

3.2.6 Loading of DOX

3 mL of a solution containing rattle-structured AuNR@mSiO₂

nanoparticles was centrifuged and dispersed in 1 mL of DI water. The solution was mixed with 300 μ L of an aqueous DOX solution (0.2 mg/mL). After stirring for 24 h in the dark, the DOX-loaded nanocapsules were precipitated through centrifugation at 15,000 rpm for 5 min. To evaluate the DOX-loading efficiency, the contents of the original and residual DOX solution in the supernatant were determined by UV-Vis measurements at 490 nm. The loading efficiency (LE%) of DOX can be calculated as follows: $LE\% = [(O_{DOX} - R_{DOX})/O_{DOX}] \times 100\%$, where O_{DOX} and R_{DOX} are the contents of the original and residual DOX solution, respectively.

3.2.7 Regrowth of gold within rattle-structured AuNR@mSiO₂

Three sets of as-prepared rattle-structured AuNR@mSiO₂ (200 μ L) solutions were mixed with 800 μ L of DI water containing a 10 mM HAuCl₄ solution in different concentrations (3 μ L, 15 μ L, and 60 μ L) under stirring to obtain three different samples. In these three samples, 24 μ L (6 μ L/min), 120 μ L (12 μ L/min), and 480 μ L (12 μ L/min) of 5 mM AA were respectively injected.

3.2.8 Characterization

The low- and high-resolution TEM images were obtained using a JEOLJEM-2100F instrument at an acceleration voltage of 200 kV, which is equipped with an EDX detector. EDX was employed for elemental composition and distribution of the AuNR@Ag core/shell NPs in the STEM mode. Field-emission scanning electron microscopic (FE-SEM) images were performed using a Hitachi S-4800 microscope. Ultraviolet-visible (UV-vis) absorption spectra were collected on a Perkin Elmer Lambda 35 spectrometer.

3.3 Results and Discussion

3.3.1 Fabrication and characterization of rattle-structured AuNR@mSiO₂ nanoparticles

The synthetic procedure for the rattle-structured AuNR@mSiO₂, as shown in Scheme 3.1, is performed in three steps. In the first step, the Au NRs are homogeneously coated with Ag using AA as a reducing agent (AuNR@Ag).^[8] Next, a mesoporous silica shell is deposited by the sol-gel method on the cetyltrimethylammonium bromide (CTAB)-stabilized AuNR@Ag core/shell nanoparticles (AuNR@Ag@mSiO₂). In the final step, Ag is selectively removed by the addition of excess hydrogen peroxide (H₂O₂).^[14]

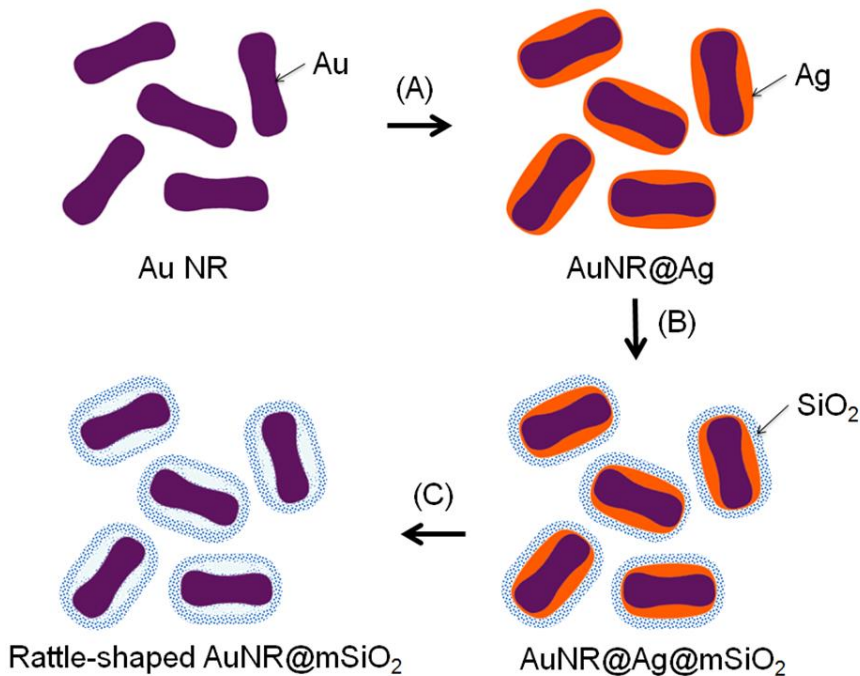
The changes in the shapes of the obtained nanomaterials at each step have been fully characterized using transmission electron microscopy (TEM). The as-prepared Au NRs were shaped similar to dog bones, being thicker at each end in comparison with the thin middle portion (Figure 3.1a). They were synthesized by using a seed-mediated growth approach in aqueous surfactant solution with the addition of sufficient AA available to reduce gold ions.^[15]

AuNR@Ag was prepared by the chemical reduction of silver nitrate

using AA as the reducing agent under alkaline conditions. At a pH of 7, AA exists as ascorbate anions, which are in the monobasic form.^[16] The ascorbate anion is the reducing species, and the concentration of ascorbate anions increases at high pH values.^[17] For this reason, silver ions could be reduced by increasing the reducing power of AA, which is achieved by elevating the pH to over 10 by adding NaOH.^[12] The color of the Au NR solution turned from purple to orange within several minutes of the addition of silver nitrate and AA. Typical TEM and scanning transmission electron microscopy (STEM) images show the epitaxial growth of the Ag nanoshell on Au NRs (Figure 3.1b). Moreover, as shown in the inset of Figure 3.1b, the STEM-energy-dispersive X-ray spectroscopy (EDS) line scan through the center of a single nanoparticle clearly shows strong Ag signals at the particle edge and strong Au signals in the particle center, which reveals a typical core-shell nanostructure. Xie *et al.* reported that a Ag shell, shaped as an orange slice, on a Au NR could be synthesized by eliminating the various ions present in the solution using purification and by adding only CTAB aqueous solution.^[11] Here, I demonstrate that oval-shaped AuNR@Ag nanoparticles can be generated by directly adding silver precursor to the as-prepared Au NR solution without any further washing step. The shell

thickness of silver was varied from 5 nm to 11 nm by varying the amount of silver nitrate from 0.001 mmol to 0.01 mmol, respectively (Figure 3.2).

Mesoporous silica shells have been successfully deposited on AuNR@Ag nanoparticles through a single-step procedure without any intermediate coating (Figure 3.1c). The formation of mesopores are strongly influenced by the CTAB molecules, which were used as the organic template to establish mesopores in the sol-gel reaction and also as the stabilizing agent in the aqueous phase.^[13] The inset in Figure 3.1c shows an expanded section of the silica shell, where the gray areas are condensed silica and the white dots are mesopores that are aligned in a disorderly manner. The silica shell thickness of the AuNR@Ag@mSiO₂ nanoparticles was modified from 8 nm to 21 nm by adjusting the amount of tetraethyl orthosilicate (Figure 3.3).



Scheme 3.1 Schematic illustration of the procedure for preparing the rattle-structured Au NR encapsulated within a mesoporous silica nanocapsule. Three main steps are (A) homogeneous coating of silver on the surface of Au NRs, (B) deposition of a mesoporous silica shell on the AuNR@Ag nanoparticles, and (C) selective etching of the silver inner layer using H₂O₂ as an oxidant of Ag.

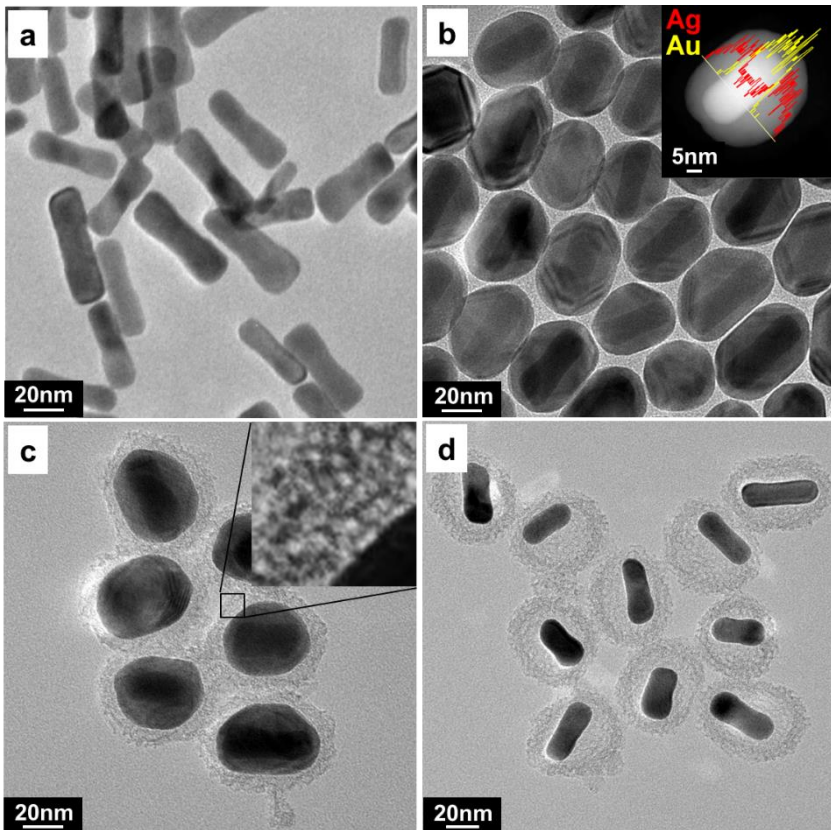


Figure 3.1 TEM images corresponding to all the steps for the fabrication of rattle-structured AuNR@mSiO₂: (a) Au NRs, (b) AuNR@Ag core/shell (inset: STEM-EDS line scan analysis), (c) AuNR@Ag@mSiO₂ core/shell/shell (inset: expanded image of the silica shell), and (d) the rattle-structured AuNR@mSiO₂ core/void/shell.

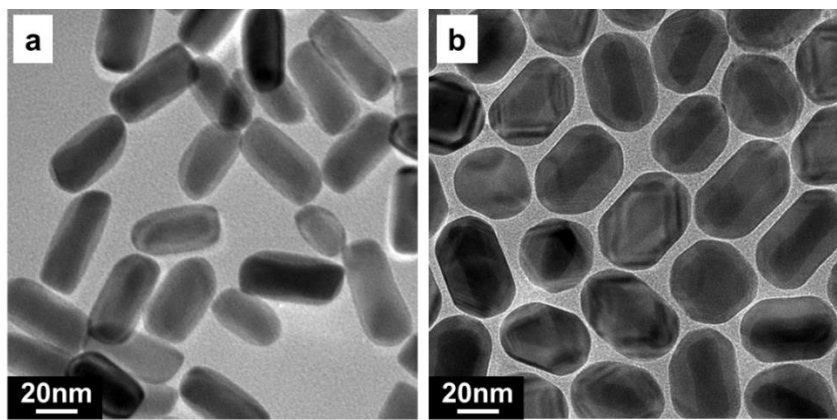


Figure 3.2 TEM images of AuNR@Ag nanoparticles with different silver shell thicknesses. The surfaces of AuNRs were coated with silver shells having thicknesses of (a) 5 nm and (b) 11 nm, obtained by adjusting the amount of AgNO_3 to 0.001 mmol and 0.01 mmol, respectively.

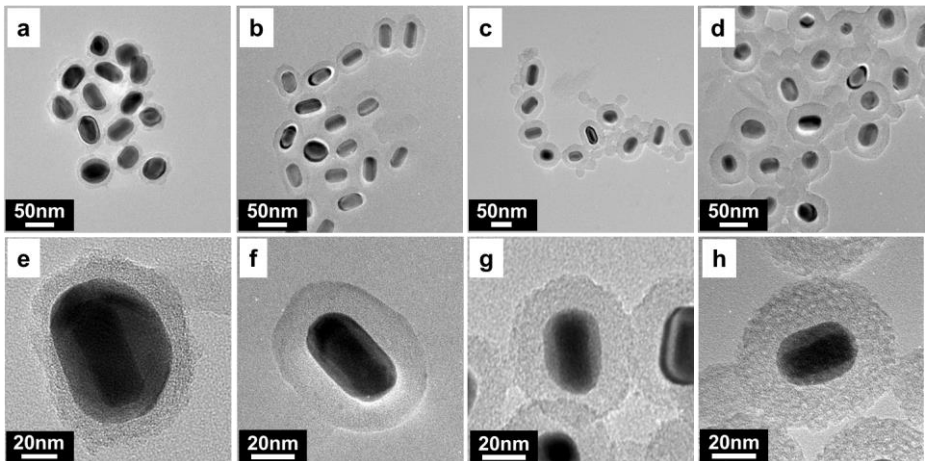


Figure 3.3 TEM images of AuNR@Ag@mSiO₂ with different SiO₂ thicknesses. The silica shell thicknesses is (a, e) 8 nm, (b, f) 14 nm, (c, g) 17 nm and (d, h) 21 nm, respectively.

To selectively remove the silver layer, H₂O₂ was used as an oxidant of Ag. H₂O₂ can be either an oxidant or a reductant depending upon the pH value of the solution. The standard redox potential of H₂O₂ is given by



Under basic conditions such as those used in these experiments, H₂O₂ is an ideal etchant for the selective removal of Ag because the standard reduction potential of H₂O₂ ($E^0 = 0.867 \text{ V}$) is higher than that of Ag⁺/Ag ($E^0 = 0.799 \text{ V}$) and lower than that of Au³⁺/Au ($E^0 = 1.51 \text{ V}$).^[14, 18] In addition, this reaction involves a color change from orange to cloudy purple, which can provide a facile colorimetric assay. The resulting cloudy purple color can be ascribed not only to the original color of the Au NRs but also to the white color of the coated silica nanoshell. Attempts were made to remove the Ag shell with different etchants such as HNO₃ and NH₄OH. Although these method can remove the silver, the mesoporous silica nanoshell is also destroyed because of their weak structural characteristics. After selectively removing the Ag interlayer with H₂O₂, the final rattle-structured Au@mSiO₂ (Figure 3.1d and

Figure 3.5) is readily dispersible in water, affording a transparent suspension (Figure 3.6). The Au@mSiO₂ is found to be stable in water over several months without adding any stabilizing reagent. The void space in the rattle-type nanostructure can be easily controlled by varying the thickness of Ag interlayer (Figure 3.7).

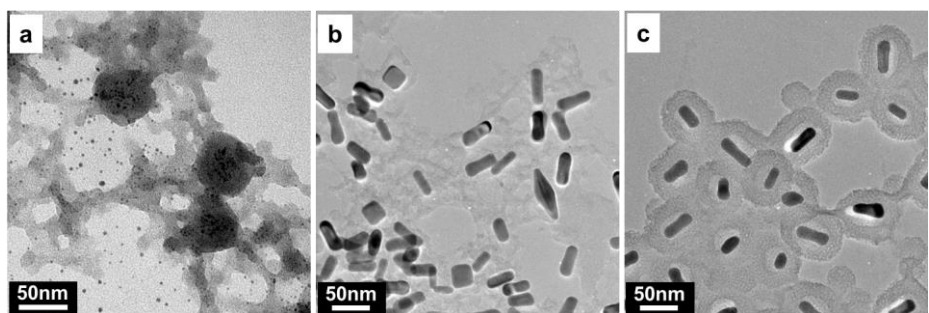


Figure 3.4 TEM images of AuNR@Ag@mSiO₂ NPs after treatment in different etchants: (a) 6 M HNO₃, (b) 5 M NH₄OH, and (c) 5 M H₂O₂.

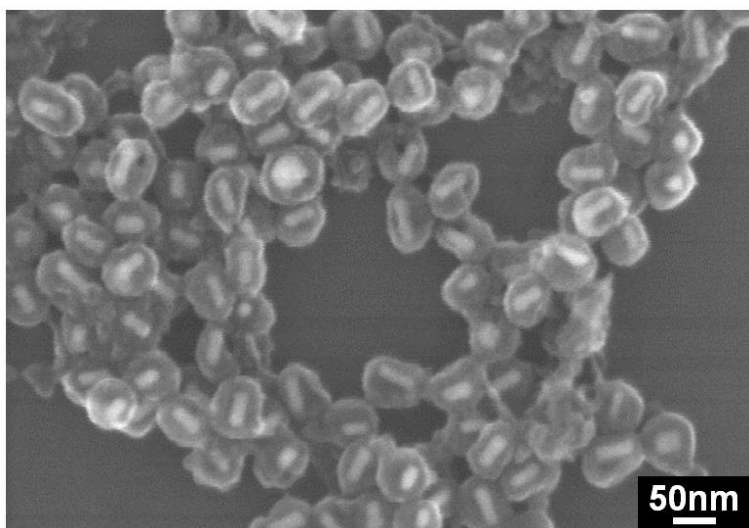


Figure 3.5 SEM image of rattle-structured AuNR@mSiO₂.

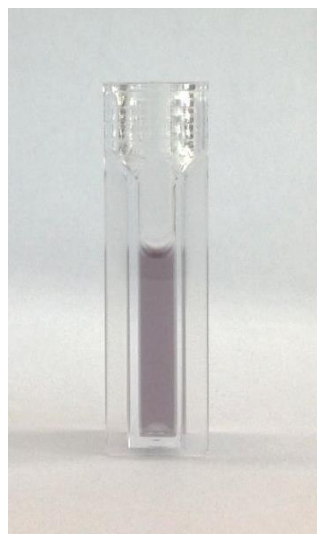


Figure 3.6 Photograph of the rattle-structured AuNR@SiO₂ dispersed in aqueous solution.

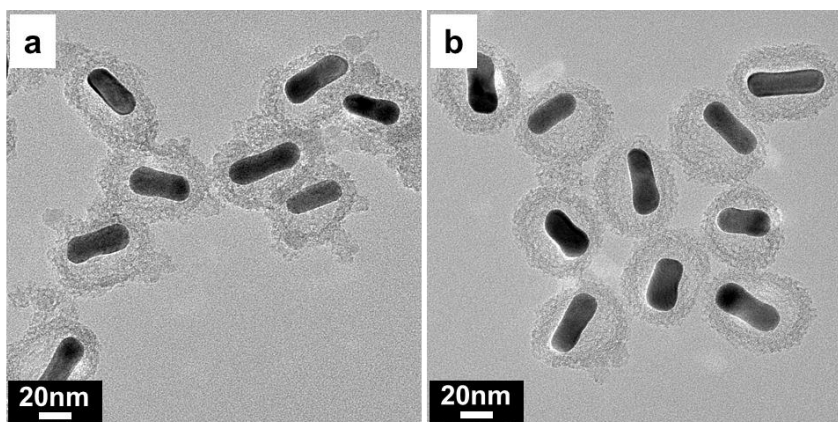


Figure 3.7 TEM images of rattle-structured AuNR@mSiO₂ with different void space: (a) 30 nm and (b) 35 nm.

During the synthesis, the dimensions of the obtained nanomaterials at each step are quite uniform (Figure 3.8) and the size distribution histograms of the nanoparticles are shown in Figure 3.9. The aspect ratio (AR) of the AuNR@Ag core-shell significantly decreased compared with that of the Au NRs. While an average AR of as-prepared Au NRs is 3.2 ± 0.4 ($49.6 \pm 5.2 \times 16.0 \pm 1.9$ nm), the AR after Ag coating is 1.4 ± 0.2 ($50.6 \pm 4.3 \times 35.3 \pm 3.2$ nm). The decrease in AR results from asymmetric coating of silver. Since Ag-Br complexes are mostly in close proximity to the lateral facets of the Au NRs, Ag is reduced more easily on the sides of the Au NRs.^[19] Afterwards, the AuNR@Ag@mSiO₂ and the rattle-structured Au@mSiO₂ show no obvious shape change and remains in the cylindrical morphology, indicating the homogeneous coating of mesoporous silica and the selective removal of silver.

The synthetic strategy described in this work has several advantages. First, although several steps are required to prepare the rattle-structured nanomaterial, washing steps are not needed between each of the steps; therefore, the complete synthesis is a consecutive process that can be finished in one pot. Second, this strategy provides easy and reproducible control of the hollow space as well as the thickness of the mesoporous silica layer. Third, the route via selective removal of the silver layer

shows good feasibility for synthesizing rattle-structured nanomaterials that maintain the original morphology of the cores.

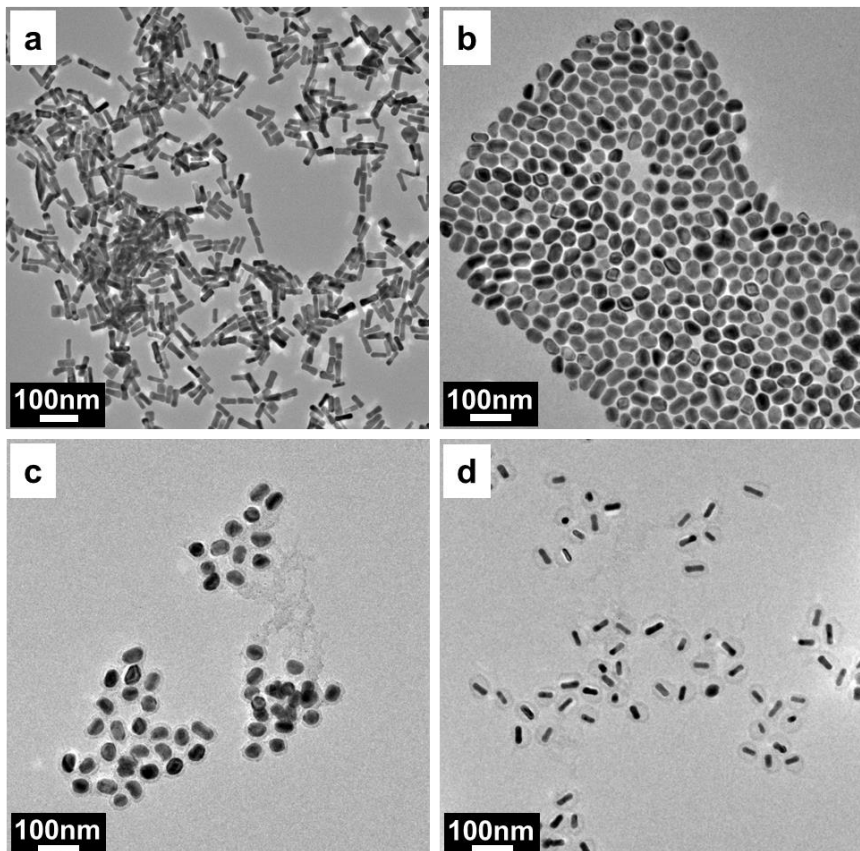


Figure 3.8 Low magnification of TEM images of (a) Au NRs, (b) AuNR@Ag core/shell, (c) AuNR @Ag@mSiO₂ core/shell/shell, and (d) the rattle-structured AuNR@mSiO₂ core/void/shell.

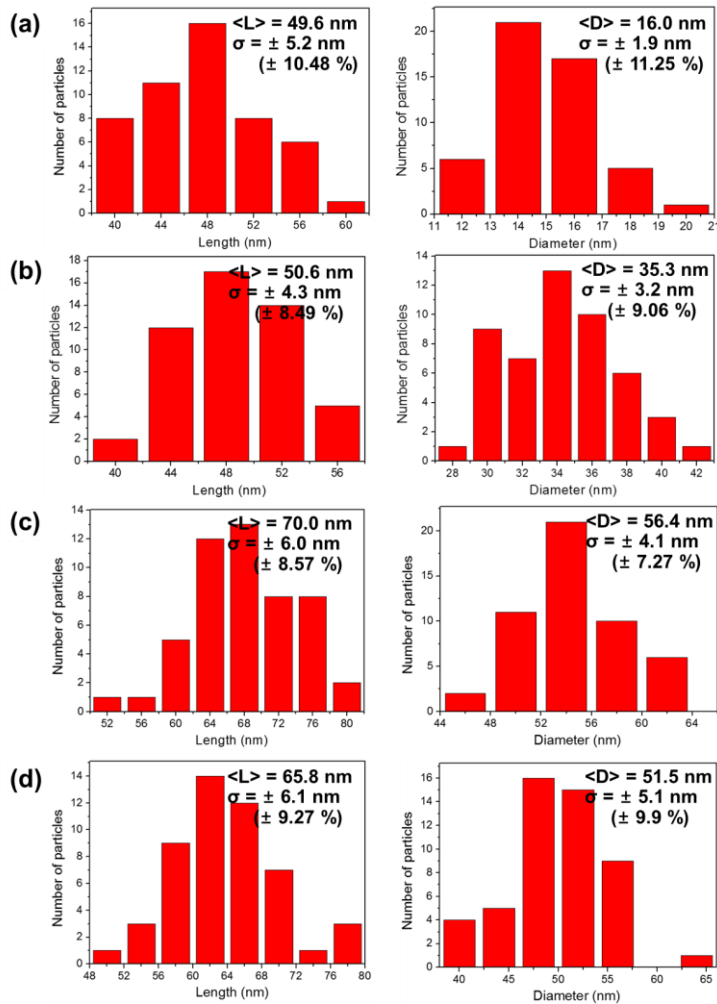


Figure 3.9 Particle size distribution histograms of (a) Au NRs, (b) AuNR@Ag core/shell, (c) AuNR @ Ag@mSiO₂ core/shell/shell, and (d) the rattle-structured AuNR@mSiO₂ core/void/shell corresponding to Figure 3.2a-d. ($\langle L \rangle$: mean length of nanorods, $\langle D \rangle$: mean diameter of nanorods, and σ : size variation and relative standard deviation of nanorods)

3.3.2 Surface plasmon resonance properties

The growth and removal of Ag on Au NRs drastically affects the UV-vis absorption spectra, as illustrated in Figure 3.10 and Figure 3.11. When the silver atoms are deposited onto NRs, four plasmon resonance peaks are observed (Figure 3.11). The plasmon peaks are numbered from low to high wavelength sequentially as peaks 1-4. Au NRs have two absorption peaks in the visible region of the spectrum, corresponding to the transverse surface plasmon resonances at around 530 nm (peak 3) and the longitudinal surface plasmon resonances (LSPR) at around 730 nm (peak 4). The peaks 1 and 2 appear on the extinction spectra when a small amount of AgNO_3 is added and reduced by AA, implying that the plasmonic properties of Ag are displayed. As the thickness of the silver shell increases, peaks 1 and 2 are very slightly red-shifted. Moreover, the spectrum of Au NRs is gradually blue-shifted and its absorption intensity is increased. As noted in previous reports, this drastic blue shift of LSPR is mainly due to the decrease in the AR and the increasing effect of the SPR properties of Ag over those of Au.^[11, 20] However, the particles maintain their rod-like morphology, and their extinction spectrum still has two absorption peaks. The two absorption peaks of AuNR@Ag at ~400 nm and ~520 nm (Figure 3.10) might be attributed to the

differences between the dielectric functions of Ag and Au, as previously reported.^[20] The increase in absorption intensity can be attributed to the increase in extinction coefficient and particle volume (Figure 3.11d). When the surface of the AuNR@Ag nanoparticles is coated with silica shell of ~9 nm thickness, the slight red shift of both peaks is related to the change in refractive index of silica and water.^[21] After eliminating silver, the rattle-structured AuNR@mSiO₂ has an almost identical absorption band of SPR with pure Au NRs.

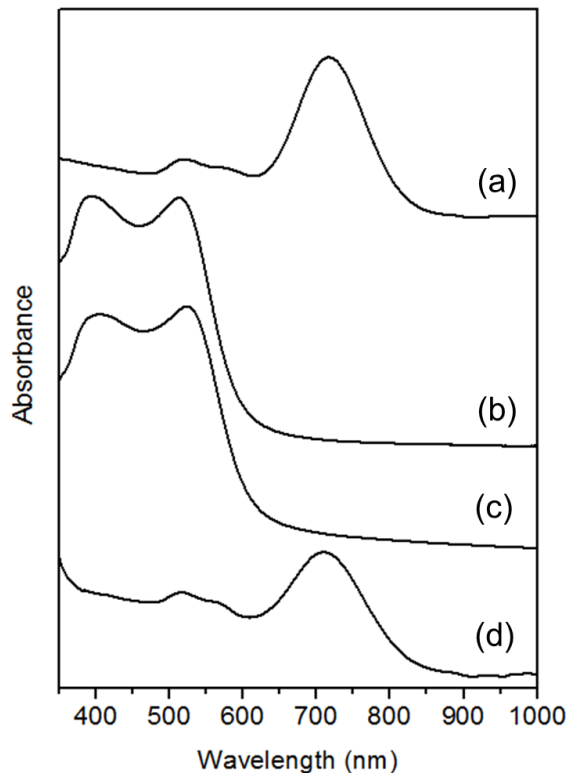


Figure 3.10 UV-vis absorption spectra of (a) Au NR, (b) AuNR@Ag core/shell, (c) AuNR@Ag@mSiO₂ core/shell/shell, and (d) the rattle-structured AuNR@mSiO₂ core/void/shell nanoparticles.

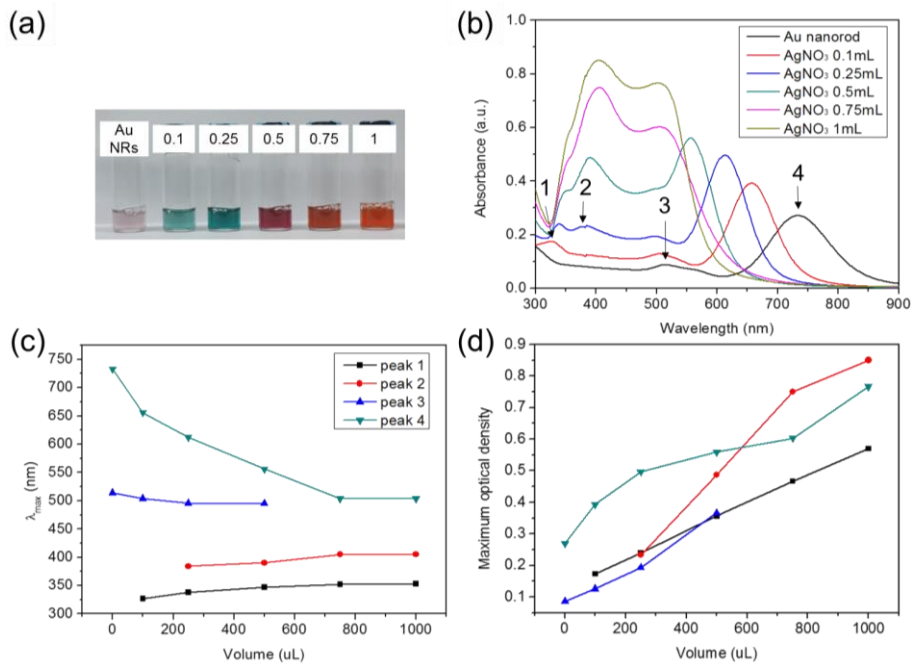


Figure 3.11 (a) Macroscopic photographs and (b) UV-vis absorption spectra of the Au NRs and the AuNR@Ag core-shell solutions. Evolutions of (c) the plasmon peak wavelengths and (d) extinction intensities of the four plasmon peaks with the AgNO₃ volume, respectively.

3.3.3 Drug loading on rattle-structured AuNR@mSiO₂ nanoparticles

The UV-vis absorption spectra recorded before and after loading the DOX into the rattle-structured AuNR@mSiO₂ are shown in Figure 3.12. The DOX loading efficiency, which can be evaluated through a comparison between the original DOX solution (0.046 mg mL⁻¹) and the residual DOX solution in the supernatant after loading into the rattle-structured AuNR@mSiO₂ (0.72 mg), reach up to 71.2%, and the drug loading content was 59.7 µg of DOX per 1 mg of support. Although the value is somewhat low compared to that of various supports, the rattle-structured nanomaterial still has the possibility as a drug carrier because of its large cavities, which include both the inner hollow space and mesopore channels (Table 3.1).

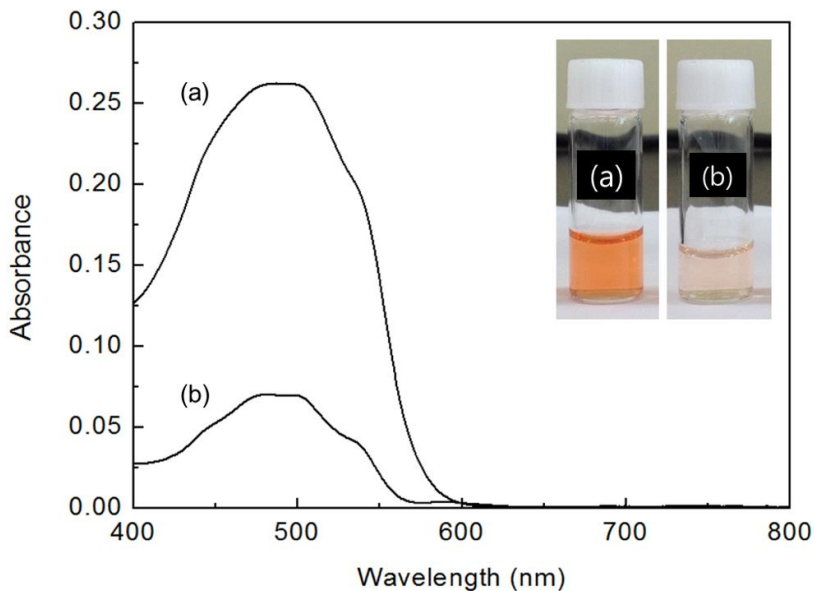


Figure 3.12 UV-vis absorption spectra of (a) the DOX solution before being loaded into the rattle-structured AuNR@mSiO₂ and (b) the DOX solution after being loaded into the nanoparticles, interacting with them, and then being unloaded from the nanoparticles. (Inset: photograph of vials containing DOX solutions corresponding to the spectra in (a) and (b). The more deeply colored solutions faded to light orange, which indicates that the DOX was loaded in the rattle-structured nanomaterials.)

Structure	Supporting material	Drug	Loading content per 1 mg of support	Ref.
Hollow structure	mSiO ₂	Doxorubicin	56 µg	[22]
	mSiO ₂	Ibuprofen	726 µg	[23]
	mSiO ₂	Doxorubicin	0.235 mg	[24]
Core/shell structure	AuNR@mSiO ₂	Fluorescein	36 µg	[9c]
	Fe ₃ O ₄ @mSiO ₂	Ibuprofen	0.18 mg	[25]
	AuNR@mSiO ₂	Doxorubicin	0.145 mg	[9d]
Rattle structure	AuNR@mSiO ₂	Doxorubicin	0.21 mg	[9e]
	Fe ₃ O ₄ @SiO ₂	Ibuprofen	0.27 mg	[2a]

Table 3.1 Comparison of the loading amounts of drug on various supports.

3.3.4 Chemical reactions in the void space

Rattle-structured AuNR@mSiO₂ can also be used as a reaction chamber in which chemical reactions are performed. Au NRs inside the mesoporous silica capsules were further grown by adding HAuCl₄ and AA into the rattle-structured nanomaterials dispersed in aqueous solution.

Considerable regrowth of Au occurred inside the confined silica capsules rather than outside. By changing the HAuCl₄ concentrations from 0.03 mM to 0.15 mM and 0.6 mM, the size of the further-grown gold cores in the silica nanocapsules was caused to gradually increase (Figure 2.13a-f). The shape of the gold cores was converted from the original rod morphology to a truncated octahedron shape. To derive the crystal structures of the gold core in silica nanocapsules, high-resolution TEM (HR-TEM) analysis of gold nanoparticles was performed. In Figure 2.13g and h, lattice fringes with a spacing of $d = 2.03 \text{ \AA}$ and 2.35 \AA are clearly visible, which can be attributed to the (200) and (111) planes of gold, respectively. This indicates that the structure of the Au nanoparticles is truncated octahedron, which corresponds to both the {111} and {100} facets.^[26] When Au NRs are regrown without silica nanocapsules, the nanoparticles are extremely aggregated (Figure 2.14). The rattle structure can provide shielding from activation between the

core nanoparticles as well as a space where the reaction can occur within the hollow nanostructure.

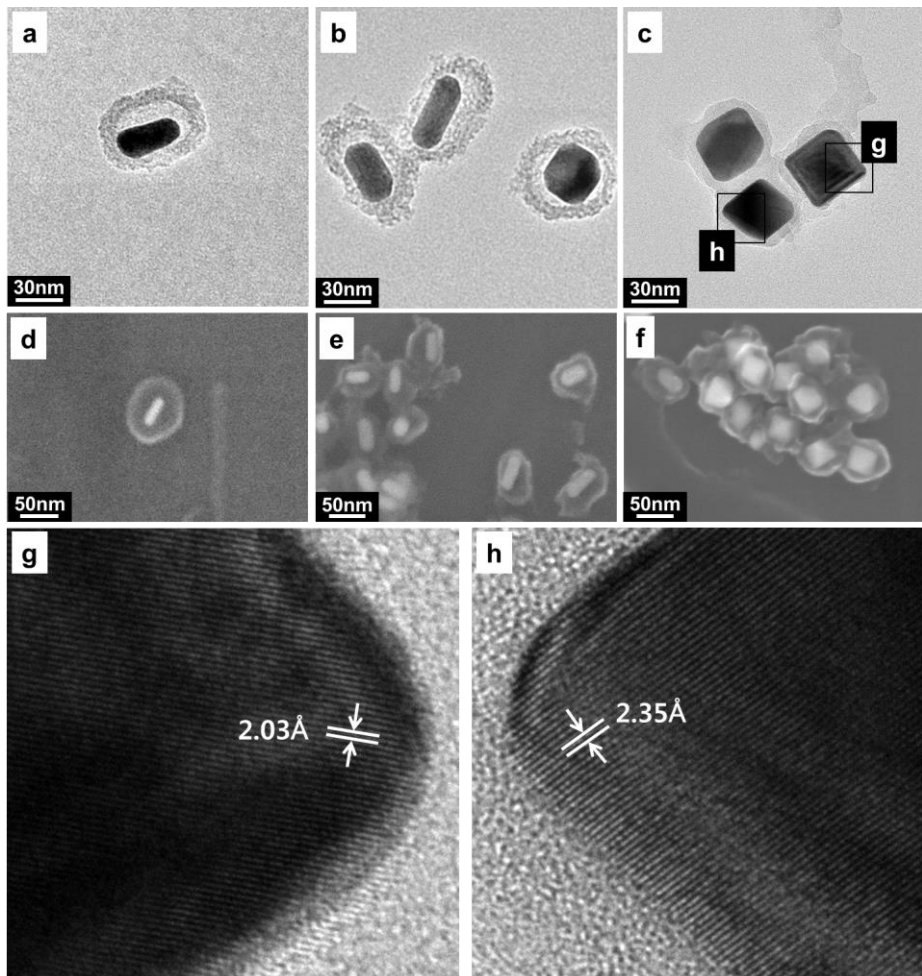


Figure 3.13 Shape evolution of gold cores grown in rattle-structured AuNR@mSiO₂. TEM and field-emission scanning electron microscopy (FE-SEM) images obtained by changing the HAuCl₄ concentrations to (a, d) 0.03 mM, (b, e) 0.15 mM, and (c, f) 0.6 mM. (g, h) HR-TEM images of the edge of the regrown Au core.

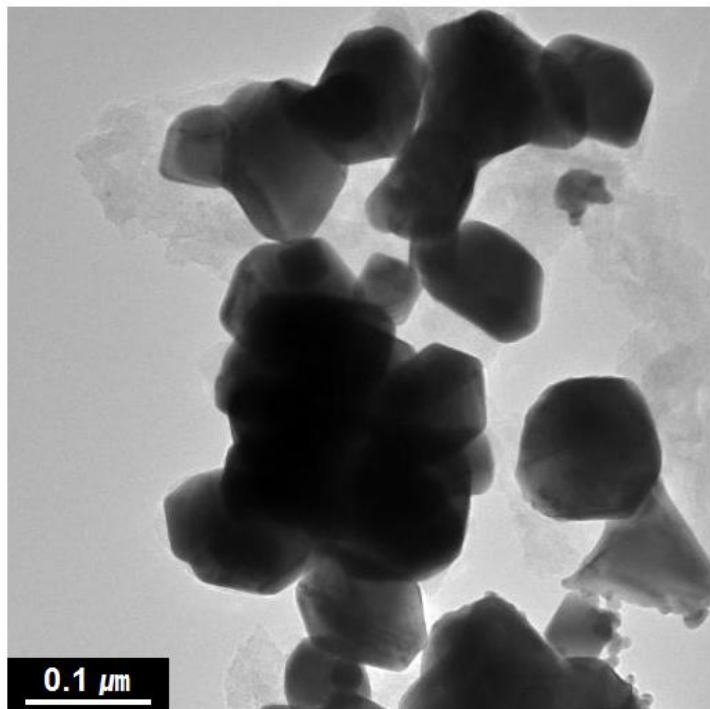


Figure 3.14 TEM image of nanoparticles regrown from AuNRs without silica nanocapsules.

3.4 Conclusion

In summary, I introduced the rattle-structured AuNR@mSiO₂ nanostructured material with a well-controlled morphology. The rattle-structured nanomaterial dispersed well in aqueous solution, and the Au NRs inside the mesoporous silica shell showed a strong absorption peak in the long-wavelength region, which was the same as that of the Au NRs themselves. Examining the drug-loading properties of the nanomaterial showed that its DOX loading content was 59.7 µg DOX per mg of the rattle-structured AuNR@mSiO₂. Additionally, the as-prepared rattle-structured nanomaterial was used to controllably regrow the core nanoparticles. The results indicate that the rattle-structured nanomaterials with well-controlled particle size and morphology have great potential for biomedical applications and as nanoreactors. The current process is highly reproducible and is expected to be extended to other nanomaterials.

References

- [1] a) Caruso, F.; Caruso, R. A.; Möhwald, H. *Science* **1998**, *282*, 1111.
b) Kim, S. W.; Kim, M.; Lee, W. Y.; Hyeon, T. *J. Am. Chem. Soc.* **2002**, *124*, 7642. c) Gross, D.; Boissière, C.; Smarsly, B.; Brezesinski, T.; Pinna, N.; Albouy, P. A.; Amenitsch, H.; Antonietti, M.; Sanchez, C. *Nature materials* **2004**, *3*, 787. d) Lou, X. W. D.; Archer, L. A.; Yang, Z. *Adv. Mater.* **2008**, *20*, 3987.
- [2] a) Hu, S.-H.; Chen, Y.-Y.; Liu, T.-C.; Tung, T.-H.; Liu, D.-M.; Chen, S.-Y. *Chem. Commun.* **2011**, *47*, 1776. b) Lee, J.; Park, J. C.; Song, H. *Adv. Mater.* **2008**, *20*, 1523. c) Buathong, S.; Ung, D.; Daou, T. J.; Ulhaq-Bouillet, C.; Pourroy, G.; Guillon, D.; Ivanova, L.; Bernhardt, I.; Bégin-Colin, S.; Donnio, B. *J. Phys. Chem. C* **2009**, *113*, 12201.
- [3] Khalavka, Y.; Becker, J.; Sönnichsen, C. *J. Am. Chem. Soc.* **2009**, *131*, 1871.
- [4] Arnal, P. M.; Comotti, M.; Schüth, F. *Angew. Chem. Int. Ed.* **2006**, *118*, 8404.
- [5] Li, H.; Bian, Z.; Zhu, J.; Zhang, D.; Li, G.; Huo, Y.; Lu, Y. *J. Am. Chem. Soc.* **2007**, *129*, 8406.

- [6] Wu, S. H.; Tseng, C. T.; Lin, Y. S.; Lin, C. H.; Hung, Y.; Mou, C. Y. *J. Mater. Chem.* **2010**, *21*, 789.
- [7] a) Slowing, I. I.; Trewyn, B. G.; Giri, S.; Lin, V. S. Y. *Adv. Funct. Mater.* **2007**, *17*, 1225. b) Zhan, Q.; Qian, J.; Li, X.; He, S. *Nanotechnology* **2010**, *21*, 055704. c) Andersson, N.; Alberius, P. C. A.; Skov Pedersen, J.; Bergström, L. *Microporous Mesoporous Mater.* **2004**, *72*, 175.
- [8] Nikoobakht, B.; El-Sayed, M. A. *Chem. Mater.* **2003**, *15*, 1957.
- [9] a) Alkilany, A. M.; Thompson, L. B.; Boulos, S. N.; Sisco, P. N.; Murphy, C. J. *Adv. Drug Del. Rev.* **2012**, *64*, 190. b) Huang, X.; Neretina, S.; El-Sayed, M. A. *Adv. Mater.* **2009**, *21*, 4880. c) Yang, X.; Liu, X.; Liu, Z.; Pu, F.; Ren, J.; Qu, X. *Adv. Mater.* **2012**, *24*, 2890. d) Zhang, Z.; Wang, L.; Wang, J.; Jiang, X.; Li, X.; Hu, Z.; Ji, Y.; Wu, X.; Chen, C. *Adv. Mater.* **2012**, *24*, 1418. e) Tang, H.; Shen, S.; Guo, J.; Chang, B.; Jiang, X.; Yang, W. *J. Mater. Chem.* **2012**, *22*, 16095.
- [10] Sau, T. K.; Murphy, C. J. *Langmuir* **2004**, *20*, 6414.
- [11] Xiang, Y.; Wu, X.; Liu, D.; Li, Z.; Chu, W.; Feng, L.; Zhang, K.; Zhou, W.; Xie, S. *Langmuir* **2008**, *24*, 3465.
- [12] Pal, T.; De, S.; Jana, N. R.; Pradhan, N.; Mandal, R.; Pal, A.; Beezer,

- A.; Mitchell, J. *Langmuir* **1998**, *14*, 4724.
- [13] Gorelikov, I.; Matsuura, N. *Nano Lett.* **2007**, *8*, 369.
- [14] Zhang, Q.; Cobley, C. M.; Zeng, J.; Wen, L.-P.; Chen, J.; Xia, Y. *J. Phys. Chem. C* **2010**, *114*, 6396.
- [15] a) Gou, L.; Murphy, C. J. *Chem. Mater.* **2005**, *17*, 3668. b) Yang, T. I.; Brown, R. N. C.; Kempel, L. C.; Kofinas, P. *J. Nanopart. Res.* **2010**, *12*, 2967.
- [16] Vasantha, V.; Chen, S. M. *J. Electroanal. Chem.* **2006**, *592*, 77.
- [17] Ambrosi, A.; Morrin, A.; Smyth, M. R.; Killard, A. J. *Anal. Chim. Acta* **2008**, *609*, 37.
- [18] Tratnyek, P. G.; Macalady, D. L. *Handbook of Property Estimation Methods for Chemicals: Environmental and Health Sciences* **2000**.
- [19] Park, K.; Drummy, L. F.; Vaia, R. A. *J. Mater. Chem.* **2011**, *21*, 15608.
- [20] Sánchez-Iglesias, A.; Carbó-Argibay, E.; Glaria, A.; Rodríguez-González, B.; Pérez-Juste, J.; Pastoriza-Santos, I.; Liz-Marzán, L. M. *Chem. Eur. J.* **2010**, *16*, 5558.
- [21] Lu, Y.; Yin, Y.; Li, Z.-Y.; Xia, Y. *Nano Lett.* **2002**, *2*, 785.
- [22] Chen, Y.; Chen, H.; Guo, L.; He, Q.; Chen, F.; Zhou, J.; Feng, J.; Shi, J. *ACS nano* **2010**, *4*, 529.

- [23] Zhao, W.; Lang, M.; Li, Y.; Li, L.; Shi, J. *J. Mater. Chem.* **2009**, *19*, 2778.
- [24] Yang, J.; Lee, J.; Kang, J.; Lee, K.; Suh, J.-S.; Yoon, H.-G.; Huh, Y.-M.; Haam, S. *Langmuir* **2008**, *24*, 3417.
- [25] Kim, J.; Lee, J. E.; Lee, J.; Yu, J. H.; Kim, B. C.; An, K.; Hwang, Y.; Shin, C.-H.; Park, J.-G.; Kim, J.; Hyeon, T. *J. Am. Chem. Soc.* **2006**, *128*, 688.
- [26] Lim, B.; Jiang, M.; Tao, J.; Camargo, P. H. C.; Zhu, Y.; Xia, Y. *Adv. Funct. Mater.* **2009**, *19*, 189.

Chapter 4. Concluding Remarks

4.1 Conclusion

Recently, the development of nanomaterials and engineering has led to the design of multi-component metallic nanomaterials with progressively increasing levels of complexity. These nanocomposite materials have not only the individual characteristics of their separate elements, but also new and unexpected properties arising from the synergistic effect between different components. However, due to the multiple components and complex structures, the manufacturing process is also complicated and limited to synthesize the specific materials. In this respect, the exploitation of facile and controlled synthetic routes towards multi-component nanomaterials with advanced properties appears to be of key importance.

In this thesis, various designed synthetic methods of multi-component metallic nanomaterials have been investigated. First, Ag-Cu core-shell and alloy bimetallic NPs were synthesized by a solventless mix-bake-wash method. The simple one-step heating process was assisted by fine salt powder as a template, obtaining small bimetallic nanomaterials. The

structures of the NPs could be tuned by the reaction temperature, allowing for selection between hetero-structured core-shell NPs and homogeneous alloys. Whereas the as-synthesized Ag@Cu core-shell NPs show a flower-like shape and consist of fcc metal Ag and Cu, including trace amounts of copper oxides, the AgCu nanoalloys show a single phase with fcc structure similar to Ag, without the copper oxide species. The synthetic strategy reported here has distinct advantages: 1) the lack of solvent makes it possible to synthesize alloys in a wide temperature window. 2) The structural morphology of core-shell versus alloy can be tuned by adjusting only the annealing temperature. 3) The proposed synthesis strategy is easily scalable for large scale production because of the low cost and simplicity of the processing procedure. This synthesis approach is expected to be capable of producing other bimetallic or trimetallic nanomaterials.

Secondly, rattle-structured nanomaterials composed of a gold NR in a mesoporous silica nanocapsule were prepared by a novel solution-based consecutive process. The rattle-structured nanomaterials were highly uniform and well dispersed in aqueous solution. In addition, the Au NRs inside the mesoporous silica shell showed a strong absorption peak in the long-wavelength region, which was the same as that of the Au NRs

themselves. The drug-loading properties of the nanomaterial and the regrowth control of the core nanoparticles were also studied. This nanomaterial is anticipated to be used as nanoreactors as well as in a variety of biological applications. The methodology in this work has several advantages: 1) a consecutive process with no need for purification steps between each of the steps can be finished in one pot. 2) The thickness of the mesoporous silica shell and the hollow space can be easily controlled by changing the amounts of each precursors. 3) The route *via* selective removal of the silver layer shows good feasibility for synthesizing rattle-structured nanomaterials that maintain the original morphology of the cores. The current process is highly reproducible and is expected to be extended to synthesize other rattle-structured nanomaterials that maintain the original morphology of the cores.

4.2 Future Aspects

The rapid progress of nanoengineering within the last several decades has enabled the creation of various multi-component nanomaterials with increasing degrees of complexity. However, although considerable advances have been made in the synthesis of multi-component nanomaterials, there are still some unresolved issues and challenges. One of the remaining challenges in nanoengineering techniques is the mass production of nanomaterials. Many of the current methods used in laboratory are effective in producing multi-component nanomaterials with narrow size distribution and well-defined structure, but scaled up fabrications usually lead to different outcomes compared to those obtained under optimal laboratory conditions. Thus, further studies must be conducted in order to develop economical and practical methods for complex nanostructures.

Another challenge is how to establish new synthetic methodologies for easy synthesis of the multi-component nanomaterials with advanced structures. Despite the tremendously great progress in synthetic techniques, most methods are generally multi-step procedures and work successfully only in a certain environment. The development of simple

and scalable methods can result in a final nanoproduct more suitable for practical applications.

Bibliography

1. International Publications

- 1) Eunjin Choi, Minjeong Kwak, Byungchul Jang, Yuanzhe Piao,
“Highly monodisperse rattle-structured nanomaterials with gold nanorod core-mesoporous silica shell as drug delivery vehicles and nanoreactors”,
Nanoscale, **2013**, *5*, 151-154.

- 2) Eunjin Choi, Sohee Lee, Yuanzhe Piao,
“A solventless mix-bake-wash approach to the facile controlled synthesis of core-shell and alloy Ag-Cu bimetallic nanoparticles”,
CrystEngComm, **2015**, *17*, 5940-5946.

- 3) Sohee Lee, Seung-Keun Park, Eunjin Choi, Yuanzhe Piao,
“Voltammetric determination of trace heavy metals using an electrochemically deposited graphene/bismuth nanocomposite film-modified glassy carbon electrode”,
Journal of Electroanalytical Chemistry, **2016**, *766*, 120-127.

- 4) Jin Gyeong Son, **Eunjin Choi**, Yuanzhe Piao, Sang Woo Han, Tae Geol Lee,
“Probing organic ligands and their binding schemes on nanocrystals by mass spectrometric and FT-IR spectroscopic imaging”,
Nanoscale, **2016**, 8, 4573-4578.
- 5) Wang Zhang, Bo Quan, Chaedong Lee, Seung-Keun Park, Xinghe Li,
Eunjin Choi, Guowang Diao, Yuanzhe Piao,
“One-step facile solvothermal synthesis of copper ferrite-graphene composite as a high-performance supercapacitor material”,
ACS Applied Materials & Interfaces, **2015**, 7, 2404-2414.
- 6) Byungchul Jang, Sungyool Bong, Seunghee Woo, Seung-Keun Park,
Jeonghyun Ha, **Eunjin Choi**, Yuanzhe Piao,
“Facile synthesis of one-dimensional iron-oxide/carbon hybrid nanostructures as electrocatalysts for oxygen reduction reaction in alkaline media”,
Journal of Nanoscience and Nanotechnology, **2014**, 14, 8852-8857.

- 7) Byungchul Jang, **Eunjin Choi**, Yuanzhe Piao,
"Preparation of well-dispersed Pt nanoparticles on solvothermal
graphene and their enhanced electrochemical properties",
Materials Research Bulletin, **2013**, *48*, 834-839.
- 8) Weon-Sik Chae, **Eunjin Choi**, Yun Ku Jung, Jin-Seung Jung, and Jin-
Kyu Lee,
"Time-resolved photoluminescence properties of semiconductor
quantum dot superlattices of different microcrystal shapes",
Applied Physics Letters, **2014**, *104*, 153101.
- 9) Seong-Gon Kim, Byung-Dong Hahn, Dong-Soo Park, Yong-Chan
Lee, **Eun-Jin Choi**, Weon-Sik Chae, Dong-Heon Baek, Je-Yong Choi,
"Aerosol deposition of hydroxyapatite and 4-hexylresorcinol coatings
on titanium alloys for dental implants",
Journal of Oral and Maxillofacial Surgery, **2011**, *69*, e354-e363.

2. International Conference

- 1) **Eunjin Choi**, Sohee Lee, Yuanzhe Piao,
“Robust thermal decomposition synthetic route to noble bimetallic
alloy nanomaterials”,
2015 International Chemical Congress of Pacific Basin Societies,
Pacificchem 2015, Honolulu, HI, USA, December 15-20, 2015.

- 2) **Eunjin Choi**, Sohee Lee, Yuanzhe Piao,
“Mix-bake-wash approach for the preparation of core-shell and alloy
Ag-Cu bimetallic nanoparticles”,
2015 International Symposium on New Frontiers in Nano-Bio
Convergence Technology, AICT, Suwon, Korea, December 17-18,
2015.

- 3) **Eunjin Choi**, Yuanzhe Piao,
“One-pot and consecutive synthesis of rattle-type gold
nanorod@mesoporous silica nanomaterials”,
The 12th International Nanotech Symposium & Nano-Convergence
Expo, NANO KOREA 2014, COEX, Seoul, Korea, July 2-4, 2014.

4) Eunjin Choi, Yuanzhe Piao,

“One-pot and consecutive synthesis of rattle-structured nanomaterials with gold nanorod@mesoporous silica for drug delivery and nanoscaled reaction”,

2014 International Symposium on New Frontiers in Nano-Bio-Energy
Convergence Science and Technology, AICT, Suwon, Korea, August
12-13, 2014. - *Oral presentation*

5) Eunjin Choi, Sohee Lee, Yuanzhe Piao,

“Solventless thermal decomposition method for the preparation of copper-based bimetallic nanoparticles”,

2014 International Symposium on New Frontiers in Nano-Bio-Energy
Convergence Science and Technology, AICT, Suwon, Korea, August
12-13, 2014.

6) Byungchul Jang, Eunjin Choi, Yuanzhe Piao,

“Well-dispersed platinum nanoparticles on graphene and their enhanced electrochemical properties”,

2014 International Symposium on New Frontiers in Nano-Bio-Energy

Convergence Science and Technology, AICT, Suwon, Korea, August
12-13, 2014.

7) **Eunjin Choi**, Yuanzhe Piao,

“Rattle structured nanomaterials of gold nanorod embedded within silica nanocapsule as drug delivery vehicles and nanoreactors”,
2013 MRS Spring Meeting & Exhibit, San Francisco, CA, USA, April
1-5, 2013. - *Oral presentation*

3. Domestic Conferences

1) **Eunjin Choi**, Sohee Lee, Dasom Kim, Yuanzhe Piao,
“Simple solventless synthesis of silver-copper bimetallic nanoparticles with core-shell and alloy structures”;
The 116th General Meeting of the Korean Chemical Society, EXCO,
Daegu, Korea, October 14-16, 2015.

2) **Eunjin Choi**, Sohee Lee, Yuanzhe Piao,

“Solventless thermal decomposition method for the synthesis of copper nanoparticles”;

2014 Spring Meeting of the Korean Society of Industrial and Engineering Chemistry, ICC, Jeju, Korea, April 30-May 2, 2014.

3) Byungchul Jang, Sungyool Bong, Eunjin Choi, Yuanzhe Piao,
“Tubular structured iron-oxide/carbon hybrid nanocomposites as an electrocatalyst for oxygen reduction reaction”,

2014 Fall Meeting of the Korean Electrochemical Society, DCC,
Daejeon, Korea, November 6-8, 2014.

4) Eunjin Choi, Yuanzhe Piao,
“Engineering rattle structures of gold nanorods encapsulated in mesoporous silica nanoparticles for drug delivery and nanoscaled reaction”,

3rd Conference on Pioneering Convergence Technologies, AICT,
Suwon, Korea, January 25, 2013.

5) Eunjin Choi, Yuanzhe Piao,
“Facile synthesis of novel rattle structured nanomaterials for drug delivery and nanoscaled reaction”,

The 111th General Meeting of the Korean Chemical Society,

KINTEX, Goyang, Korea, April 17-19, 2013.

- 6) Byungchul Jang, Eunjin Choi, Yuanzhe Piao,
“Synthesis of Pt/Graphene composite materials *via* solvothermal and
polyol process”,
The 1st Conference on Pioneering Convergence Technologies,
Ramada Hotel, Jeju, Korea, February 14-16, 2011.

4. Patents

- 1) 박원철, 최은진, 이소희, “복합 금속 나노 입자의 제조 방법”,
출원번호: 10-2014-0051526.

5. Award

- Excellent Paper Presentation Award at the 2014 Spring Meeting of the
Korean Society of Industrial and Engineering Chemistry.



KSIEC 2014-066

Excellent Paper Presentation Award

May 1, 2014

최운진·이소희·박원철†
서울대학교

On behalf of the Korean Society
of Industrial and Engineering
Chemistry (KSIEC), I hereby present
you this award for an excellent
Poster presentation of the paper at
the 2014 KSIEC Spring meeting.

Paper Title: Solventless Thermal Decomposition
Method for the Synthesis of Copper
Nanoparticles

Kim, Chong-Don
President,
The Korean Society of Industrial and
Engineering Chemistry



국 문 초 록

귀금속 나노입자는 입자의 크기, 모양, 화학적 조성에 따라 독특한 물리적, 화학적 성질을 띠는 물질이다. 지난 반세기 동안 균일한 나노입자를 제조하기 위해 다양한 합성기술이 개발되었고, 크기와 모양을 제어하는 연구가 주를 이뤄왔다. 최근에는 나노재료의 보다 효율적인 응용을 위해 다성분계 금속 나노물질에 대한 연구가 많은 관심을 받고 있다. 나노복합물질은 각 구성성분의 성질을 하나의 입자에 내포시킬 수 있을 뿐만 아니라, 서로 다른 구성물질간의 상호작용으로 인해 새로운 성질 또는 우수한 성질을 가질 수 있다는 장점이 있다. 본 학위 논문에서는 다성분계 금속 나노물질의 간편한 합성기술과 구조제어 연구에 대해 기술하였다.

첫째로, 은-구리 이종금속 나노입자를 한 번의 공정으로 합성할 수 있는 건식공정법을 개발하였다. 입자의 응집을 억제하고 작은 크기의 나노입자를 제조하기 위해 금속염 분말을 지지체로 사용하였고, 반응온도를 조절함에 따라 코어-쉘 구조와 합금구조를 손쉽게 제어할 수 있었다. 제조된 은-구리 코어-쉘 나노입자는 미량의 산화구리가 포함되어 있는 반면, 은-구리

합금나노입자는 산화구리가 존재하지 않으면 은과 같은 결정 구조를 갖는다는 것을 확인하였다. 또한 순환전압전류법 측정을 통해 은-구리 합금나노입자의 표면은 상대적으로 낮은 구리함유량을 갖고 있고, 합금화를 통해 산화안정성이 향상된다 는 것을 보여주었다.

두번째로, 금 나노막대와 실리카 나노캡슐로 구성된 래틀구조의 나노재료를 단일반응기에서 합성할 수 있는 방법을 개발하였다. 이 합성법은 수용액 상에서 금 나노막대에 은을 코팅하고, 실리카를 추가로 코팅한 후, 중간층인 은을 선택적으로 제거하는 하드템플레이트 방법을 기반으로 하였다. 제조된 래틀 구조의 금 나노막대-실리카 나노복합체는 균일한 크기를 가지며, 그의 분광학적 특성은 단일 금 나노막대와 유사한 장파장 영역에서 강한 흡수 피크가 나타나는 것을 볼 수 있었다. 또한 은과 실리카의 전구체 양을 조절함에 따라 내부의 빈 공간과 실리카 껍질 두께를 손쉽게 조절할 수 있었다. 이 나노구조체를 이용하여 약물담지체와 나노반응기로서의 응용 가능성 을 확인하였다.

주요어: 다성분계 나노물질, 귀금속, 합성, 구조 제어, 코어-쉘,
합금, 래틀 구조.

학 번: 2010-23946